Citation (APA)
Sattari, M., Luckabauer, M., Ebrahimi, A., & R.B.E. Römer, G. W. (2026). Computational study of laser beam shaping in directed energy deposition using a thermal-fluid – Microstructure model. *Journal of Materials Research and Technology*, *41*, 7168-7194. https://doi.org/10.1016/j.jmrt.2026.02.190

Journal of Materials Research and Technology 41 (2026) 7168–7194

Contents lists available at ScienceDirect

Journal of Materials Research and Technology

journal homepage: www.elsevier.com/locate/jmrt

Computational study of laser beam shaping in directed energy deposition using a thermal-fluid – Microstructure model

Mohammad Sattari [a,*], Martin Luckabauer [a], Amin Ebrahimi [b,c], Gert-willem R.B.E. Römer [a]

[a] Department of Mechanics of Solids, Surfaces and Systems (MS^3), Faculty of Engineering Technology, University of Twente, Drienerlolaan 5, 7522NB Enschede, the Netherlands
[b] Department of Materials Science and Engineering, Faculty of Mechanical Engineering, Delft University of Technology, Mekelweg 2, 2628CD Delft, the Netherlands
[c] TNO (Netherlands Organisation for Applied Scientific Research), Stieltjesweg 1, 2628 CK Delft, the Netherlands

ARTICLE INFO

Keywords:
Laser beam shaping
Grain morphology control
Solidification microstructure
Process-structure relationships
Metal additive manufacturing
Microstructure prediction

ABSTRACT

Laser beam shaping significantly influences solidification microstructure evolution in directed energy deposition (DED-LB), with distinct effects on grain morphology and crystallographic texture. To enable quantitative prediction and mechanistic understanding of these beam shaping effects on solidification microstructure evolution in both welding and metal additive manufacturing, an optimized thermal-fluid – microstructure coupling framework was developed. The integrated model incorporates novel features, including spatiotemporal optimization, efficient thermal-to-microstructural data interpolation (158x faster), CPU-parallelized grain growth algorithms (3.17x speedup), and adaptive time-step size calculation. Single-track experiments and corresponding simulations were performed for both laser-induced melting and laser-based directed energy deposition (DED-LB) using uniform circular and uniform square laser beam intensity profiles. The resulting crystallographic texture and grain morphology were quantitatively characterized through cross-sectional analysis, pole figures, and statistical distributions. Excellent agreement was achieved between experiments and simulations, with texture index deviations below 10.8% and accurate reproduction of grain size distributions demonstrating the model's fidelity. For the chosen process parameters, the two beam shapes have measurable but limited influence on texture development, with variations ranging from −5.3% to +5.1%. However, beam shape had a much stronger impact on grain morphology than on texture: circular beams refined the bulk grain-area and aspect-ratio distributions relative to square beams, while square beams yielded smaller mean grain areas, highlighting the need for distribution-level metrics beyond simple averages. By linking these morphological trends to beam-shape-dependent variations, the presented framework serves as a predictive tool for microstructure-aware process optimization in laser-based additive manufacturing.

Nomenclature

α	Thermal diffusivity	$m^2 \cdot s^{-1}$
α_t	Time fraction covered by the Cellular Automata simulation time between two thermal time-steps	-
Γ	Gibbs–Thompson coefficient	K·m
ΔH_f	Enthalpy of fusion per unit mass	$J \cdot kg^{-1}$
ΔT	Undercooling	K
ΔT_σ	Standard deviation undercooling	K
ΔT_C	Compositional undercooling	K
ΔT_{cr}	Critical undercooling of the potential nucleation site	K
ΔT_{growth}	Grain growth undercooling	K
ΔT_K	Kinetic undercooling	K
ΔT_N	Mean undercooling	K
ΔT_s	Solidification undercooling	K
ΔT_R	Curvature undercooling	K
ΔT_T	Thermal undercooling	K
Δt_{CA}	Size of the Cellular Automata time-step	s
$\Delta t_{CA,jump}$	Initial Cellular Automata time jump	s
Δt_{max}	Upper limit for Cellular Automata time-step size	s
Δx	Cellular Automata cell size	m
θ	Angle between the laser beam scanning direction and the maximum heat flow direction	rad
μ	Index of the growing cell	-
μ_K	Interface kinetic coefficient	$m \cdot K^{-1} \cdot s^{-1}$
ν	Index of the captured cell	-
ξ_t	Thermal stability parameter	-

(continued on next page)

---

* Corresponding author.
E-mail address: m.sattari@utwente.nl (M. Sattari).

https://doi.org/10.1016/j.jmrt.2026.02.190
Received 4 January 2026; Received in revised form 21 February 2026; Accepted 22 February 2026
Available online 1 March 2026

(*continued*)

ξ_c	Solute stability parameter	-
ρ	Material density at the liquidus temperature	$kg{\cdot}m^{-3}$
σ^*	Stability parameter	-
τ	Time-step	-
$\tau_{th,nuc1}$	Thermal time-step of the first nucleation	-
ϕ	Euler rotation angle around the x-axis	rad
φ	Euler rotation angle around the z-axis	rad
ψ	Angle between the crystallographic orientation of the nucleus and the solidification front velocity vector	rad
A	Area	m^2
a	Interatomic spacing	m
C_0	Nominal solute concentration	wt%
C_μ	Center coordinates of the capturing octahedron	m
C_ν	Center coordinates of the octahedron within the captured cell	m
c_ν	Local center coordinates of the octahedron within the captured cell	m
C_l^*	Solute concentration in the liquid at the interface	wt%
C_s^*	Solute concentration in the solid at the interface	wt%
c_p	Specific heat of the liquid	$J{\cdot}kg^{-1}$
CA	Microstructure-related index	-
CHD	Deviation from the convex hull	-
D_{KS}	Kolmogorov–Smirnov distance	-
D_l	Chemical diffusivity	$m^2{\cdot}s^{-1}$
$E_1(P)$	Exponential integral function of the first kind	-
G	Temperature gradient	$K{\cdot}m^{-1}$
I	Projected point	m
I_g	Grain index	-
I_s	Cell state	-
$I_v(P)$	Ivantsov function	-
J	Projected point	m
k	Kinetic partition coefficient	-
k_e	Equilibrium partition coefficient	-
k_{th}	Thermal conductivity	$W{\cdot}m^{-1}{\cdot}K^{-1}$
$L_{1j=2:3}$	Octahedron specific lengths	m
L_ν	Initial size of the octahedron within the captured cell	m
L_g	Octahedron size	m
M	Metal fraction	-
M_{rot}	Rotation matrix	-
M_{cr}	Critical metal fraction	-
m	Kinetic liquidus slope	$K{\cdot}wt\%^{-1}$
m_e	Equilibrium liquidus slope	$K{\cdot}wt\%^{-1}$
Nt	Time fraction	-
N_V	Nucleation density	m^{-3}
n	Volume unit (node or cell) number	-
$\overrightarrow{n_s}$	Unit normal vector	m
$n_{th,nuc}$	Index list of the metal nodes with a temperature higher than $T_{nuc,min}$	-
$n_{th,nuc1}$	Index list of the nodes among the $n_{th,nuc}$ nodes that will cool down below $T_{nuc,min}$	-
n_V	Number of potential nucleation sites	-
O_g	Grain crystallographic orientation	rad
$\boldsymbol{OC}$	Matrix of repeated grain center coordinates	m
$\boldsymbol{OV}$	Matrix of octahedron vertices coordinates	m
$\boldsymbol{OV}_{unit}$	Matrix of unit octahedron vertices coordinates	m
P	Perimeter	m
P_ν	Projected point	m
P_c	Solute Peclet number	-
P_t	Thermal Peclet number	-
p	Nodal property	-
p_{KS}	Kolmogorov–Smirnov significance	-
p_{cell}	Cell's property	-
R	Solidification front velocity	$m{\cdot}s^{-1}$
$\boldsymbol{R}_{X,\phi}$	Rotation matrix around the x-axis for ϕ radians	-
$\boldsymbol{R}_{Z,\varphi_1}$	Rotation matrix around the z-axis for φ_1 radians	-
$\boldsymbol{R}_{Z,\varphi_2}$	Rotation matrix around the z-axis for φ_2 radians	-
$\boldsymbol{R}_{ZXZ}$	Rotation matrix	-
r	Barycentric coordinates	-
r_{tip}	Dendrite tip radius	m
$S_{i=1:3}$	Three nearest vertices of the growing octahedron to the center of the captured cell	m
T	Temperature	K
T_l	Liquidus temperature	K
$\dot{T}_{max,\tau_{th}}$	Maximum cooling rate among the $n_{th,nuc}$ nodes	$K{\cdot}s^{-1}$
$T_{nuc,max}$	Maximum temperature of nucleation	K
$T_{nuc,min}$	Minimum temperature of nucleation	K
T_s	Solidus temperature	K
t	Time	s
$t_{th,last}$	Total thermal time	s
th	Thermal index	-
V_{CA}	Cellular Automata domain volume	m^3
v	Velocity	m/s
v_D	Solute trapping velocity	$m{\cdot}s^{-1}$
v_l	Scanning velocity of the laser beam	$m{\cdot}s^{-1}$
v_{tip}	Dendrite tip growth velocity	$m{\cdot}s^{-1}$
$v_{tip,max}$	Maximum dendrite tip growth velocity	$m{\cdot}s^{-1}$
X	Cartesian unit volume center coordinates	m
X_g	Octahedron center coordinates	m
X_μ	Center coordinates of the growing cell	m
X_ν	Center coordinates of the captured cell	m
x_ν	Local center coordinates of the captured cell	m

(*continued on next column*)

1. Introduction

Metal additive manufacturing (AM) has emerged as a revolutionary technology for fabricating high-performance components [1,2]. Among the various AM methodologies, laser-based Directed Energy Deposition (DED-LB) stands out as an efficient approach for layer-wise fabrication of relatively large and complex metallic structures [1,3]. In one approach, DED-LB involves the precise deposition of metal powder, transported by a carrier gas through a nozzle, onto a substrate where it is melted by a high-power laser beam as the energy source [1]. This process is schematically illustrated in Fig. 1. Typically, shielding gas is supplied to the laser-material interaction zone to prevent oxidation of the hot material [4]. The interaction between the laser beam and the material (both powder and substrate) in DED-LB is a complex interplay of thermal, fluidic, and metallurgical phenomena, making DED-LB a subject of intense research and development in the field of AM [3,5].

The solidification microstructure significantly affects the mechanical properties of the deposited material by governing grain morphology, crystallographic texture, and defect sensitivity—for many materials, such as nickel-based superalloys, titanium aluminides, aluminum alloys, pure molybdenum, and steels [6–8]. In DED-LB, large temperature gradients (as high as about 10^6 K/m [9]) and rapid solidification velocities (as high as about 10^5 K/s [10]) promote the growth of elongated columnar grains aligned with the build direction [11–13]. Such microstructure introduces significant performance challenges, including anisotropic mechanical behavior and increased susceptibility to crack initiation [14,15]. Controlling the microstructure, particularly aiming for equiaxed grains, is a major goal for enhancing the isotropy and mechanical reliability (greater resistance to cracking) of AM parts [16–18]. Producing equiaxed morphologies requires control over the solidification process, particularly control over the temperature gradient (G) and the solidification rate (R), as these quantities determine the stability of the solid-liquid interface [19–21].

DED-LB exhibits fundamentally different beam shaping effects compared to powder bed fusion (PBF-LB/M), necessitating process-

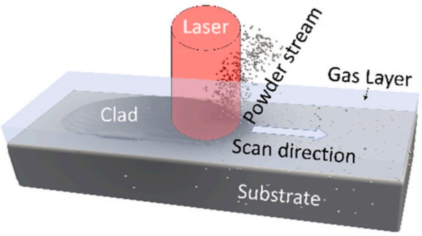

Fig. 1. Schematic representation of the DED-LB process. A laser beam (red) scans across the substrate, generating a melt pool that melts incoming powder particles to form a clad track. The light blue region represents the gas layer, comprising both the particle-carrier gas and the shielding gas to prevent oxidation.

specific optimization strategies [22,23]. DED employs directed powder nozzles creating material addition with deep non-flat melt pools and strong substrate coupling through significant conduction, whereas PBF-LB/M uses pre-spread powder beds producing shallow melt pools with layer-by-layer remelting and minimal substrate interaction [24,25]. DED-LB's higher deposition rates, larger beam spots, and lower cooling rates result in coarser microstructures and higher dilution, while PBF-LB/M achieves finer microstructures through rapid cooling and precise layer control [23]. Literature on PBF-LB/M beam shaping cannot be directly transferred to DED-LB due to these differences in melt pool dynamics, thermal gradients, and material delivery, making specific beam shaping studies essential for DED-LB [25–28].

Recent laser-based material processing studies have demonstrated the critical influence of thermal conditions on solidification microstructure. Xie et al. showed that laser cladding versus vacuum cladding of high-entropy alloy coatings produces distinct dendritic structures through variations in thermal gradient and cooling rate [29,30], while laser power modulation directly controls crystallinity and grain-boundary defect density [31]. Similarly, laser surface treatment investigations revealed that processing parameters significantly affect microstructure transformation and mechanical properties, with different baseline structures responding distinctly to identical laser conditions [32]. These thermal processing effects on microstructure-property relationships extend to other controlled cooling regimes, such as cryogenic treatments that enhance grain refinement and mechanical performance [33]. These findings confirm that thermal-fluid dynamics fundamentally govern grain morphology and texture—principles directly applicable to beam shaping strategies in DED-LB.

Controlling solidification microstructure through laser beam shaping represents a promising yet incompletely understood strategy for tailoring grain morphology and mechanical isotropy in metal additive manufacturing. Progress in this area is hindered by the lack of quantitative, beam-shape-resolved G and R maps and their direct linkage to grain morphology and texture in DED-LB, as well as by the high computational cost associated with full-track CA-coupled predictions under realistic thermal-fluid conditions. Laser beam shaping—deliberate modifications to the spatial intensity profile of the laser beam—offers advanced control over localized heat distribution without altering overall process parameters [34,35]. Recent experimental studies have demonstrated that non-Gaussian beam profiles such as square, annular, and elliptical shapes can significantly alter grain structure outcomes [1,16,18,36]; however, quantitative mechanistic understanding of how beam profile variations influence solidification parameters (temperature gradient G, solidification rate R, and their dimensionless ratios governing grain morphology) remains limited in the literature, particularly for directed energy deposition processes. This knowledge gap motivated the present investigation. Laser beam shaping alters melt pool geometry and solidification dynamics by redistributing the input laser energy. The majority of existing grain structure models for DED-LB or laser welding processes assume a conventional Gaussian or circular laser intensity profile [28,37]. Only recently researchers have started to investigate how altering the beam profile influences the predicted microstructure. For example, Shi et al. [18] demonstrated that transverse elliptical beams widen the melt pool and increase the undercooled volume, enhancing equiaxed grain nucleation. In our previous work, we [1] confirmed via thermal-fluid simulations that compared to uniform circular beam profiles, beams with a uniform square intensity profile generate a larger melt pool with flatter temperature gradients and more uniform fluid flow convection patterns. Consistent with these predictions, Bremer et al. [16] found that square beam profiles significantly increase the equiaxed grain fraction, compared to circular beams, in experimental DED builds. Further, Vidergar et al. [36] found that when comparing uniform circular, Gaussian, and annular profiles that annular beams deliver energy more evenly across the melt pool, reducing porosity and stabilizing grain structure.

The accurate prediction of solidification microstructure in AM faces several inherent challenges due to the complexity of the thermophysical phenomena and extreme processing conditions. Among the most widely used approaches to simulation microstructure formation, the Cellular Automata (CA) method [38], often coupled with Finite Element (FE) or Finite Volume (FV) methods to simulate the thermal-fluid phenomena, strikes a balance between computational efficiency and physical fidelity [4,11,39,40]. The combined modeling approach leverages the strengths of each method: the thermal-fluid model addresses process physics with high accuracy, while the CA model efficiently predicts microstructural features such as grain size, morphology, and crystallographic texture [3,5,11,17,18,20,21,41–45]. Conventional CA models coupled with FE or analytical thermal models often neglect complex melt pool phenomena such as Marangoni convection, keyholing, and surface instabilities, which significantly affect local thermal profiles and therefore grain morphology [14]. Rolchigo et al. [46] highlighted the impact of mesh and time-step size on grain selection accuracy. Fine resolution is essential for capturing grain competition in high-gradient regions. Therefore, multi-scale frameworks combining CA with thermal-fluid models have been proposed to overcome these limitations, but at the expense of dramatically increased computational cost [13,20]. Thus, while CA-based models have proven essential for microstructure prediction in AM, continuous refinement in computational efficiency remains crucial to achieving predictive reliability.

This investigation pursues three interconnected objectives: (1) Quantify and mechanistically explain the effects of laser beam intensity profile (specifically, uniform circular vs. square profiles) on solidification grain morphology, crystallographic texture, and key thermal parameters (G/R, $G{\cdot}R$) during directed energy deposition, thereby establishing fundamental design guidelines for beam shaping optimization. (2) Develop a computationally optimized thermal-fluid—microstructure coupling framework incorporating novel algorithms for CPU parallelization of grain growth calculations, spatiotemporal optimization of thermal-to-microstructure property interpolation reducing memory requirements, while maintaining numerical accuracy, fast trilinear interpolation schemes for efficient data transfer between non-conforming meshes, and adaptive time-stepping to enable tractable high-resolution grain-scale prediction. (3) Validate the framework through quantitative comparison with electron backscatter diffraction measurements, pole figure analysis, and grain morphology statistics for single-track laser melting and directed energy deposition using uniform circular and square laser beam intensity profiles, establishing the model as a reliable tool for predictive exploration of beam shaping strategies in metal AM.

2. Models

Microstructure modeling heavily relies on accurately approximating the laser-induced spatiotemporal thermal profile during the DED-LB process. Achieving an adequate level of accuracy in predicting the thermal profile evolution, to be used in a microstructure model, is challenging when using thermal models that neglect the dynamics of molten metal flow [1,47]. In our work [1], we developed an enhanced thermal-fluid model requiring no tuning parameters that allows for the prediction of spatial and temporal thermal profiles induced by the absorbed laser energy with a level of accuracy required for microstructure modeling. In the following, this thermal-fluid model is briefly introduced and summarized. Subsequently, the thermal-fluid model is coupled with a numerical solidification microstructure CA model, which introduces novel approaches to expedite grain nucleation and growth computations.

2.1. *Thermal-fluid model*

Mathematically, the three-dimensional spatiotemporal temperature distribution, as well as the melt pool dynamics, during a single-track DED-LB process of 316L austenitic stainless steel, are described by three conservation equations (of mass, momentum, and energy), as well as by the free surface advection equation, as described in our earlier work [1]. The coupled equations were numerically solved using the discrete element method (DEM), finite volume method (FVM), and volume of fluid (VoF) technique [1]. The thermal-fluid model includes an enhanced optical attenuation model to account for the "shadowing" effects of powder particles traveling through the laser beam towards the laser-induced melt pool, on the power and energy density distribution of the laser beam in the focal plane. Further, the model considers the temperature and incident angle dependent laser energy absorption, as well as the temperature and alloy element composition dependent surface tension. Next, this model was used to investigate the effect of the laser beam intensity profiles (circular, ring (annular), and square, all with uniform intensity profiles) on the spatiotemporal temperature distribution of the laser-material interaction zone during DED-LB of austenitic stainless steel (AISI 316L). Experimental validation was performed by measuring deposited track dimensions for three different laser beam shapes in the laser focal spot.

In the model, the thermal-fluid profile in the laser-induced melt pool is characterized by nodal coordinates, $X(n_{th})$, temperature, $T(n_{th}, \tau_{th})$, fluid fraction, $M(n_{th}, \tau_{th})$, hereafter referred to as metal fraction, and the calculation time, $t(\tau_{th})$, where n_{th} and τ_{th} denote the node number and thermal time-step, respectively. The metal fraction M represents the volume ratio of the unit volume occupied by metal to the total unit volume, including gas. A metal fraction value of zero signifies that the unit volume contains gas only, while a value of one indicates that the unit volume is fully occupied by metal. A value between zero and one suggests that the unit volume is located at the gas-metal interface (the free surface) [1]. In the model, nodes are considered to be the central point of thermal unit volumes. The location of the nodes is determined by three fixed Cartesian coordinates, represented as $X(n_{th})$.

The thermal-fluid model was previously validated against experimental melt pool dimensions and DED-LB track heights in Ref. [1]. As shown in Fig. 2, for laser melting, predicted melt pool widths and depths showed deviations of 4.3%, 0.9% (circular beam) and 4.0%, 3.2% (square beam) from measurements. For DED-LB, predicted melt pool depths, widths, and track heights showed deviations of 7.7%, 0.8%, 1.6% (circular beam) and 8.4%, 4.1%, 1.6% (square beam). These results accurately captured the trend of shallower, wider melt pools and comparable track heights for square beams versus narrower, deeper pools for circular beams, as described in Ref. [1].

2.2. Microstructure model

The use of an explicit Cellular Automata (CA) microstructure modeling methodology facilitates a comprehensive evaluation of the effect of laser beam intensity profile on microstructure evolution and material characteristics during solidification in DED-LB [46]. Considering that the main focus of the present study is on the crystallographic texture and grain analysis resulting from variations in the laser beam intensity profile, the CA methodology is the most suitable approach to study microstructure information at the grain scale, particularly the meso-scale [11]. This choice reduces computational requirements significantly relative to simulations at the dendrite-arm scale, allowing for the simulation of millions of grains in the domain of interest [2]. Moreover, at the meso-scale level, sub-grain data is disregarded, and it is assumed that the grain growth velocity equals the dendritic tip velocity [48]. Thus, the CA model can effectively capture the dynamic interplay among nucleation, growth, and solidification of individual grains, facilitating the investigation of the underlying mechanisms driving microstructure development [21].

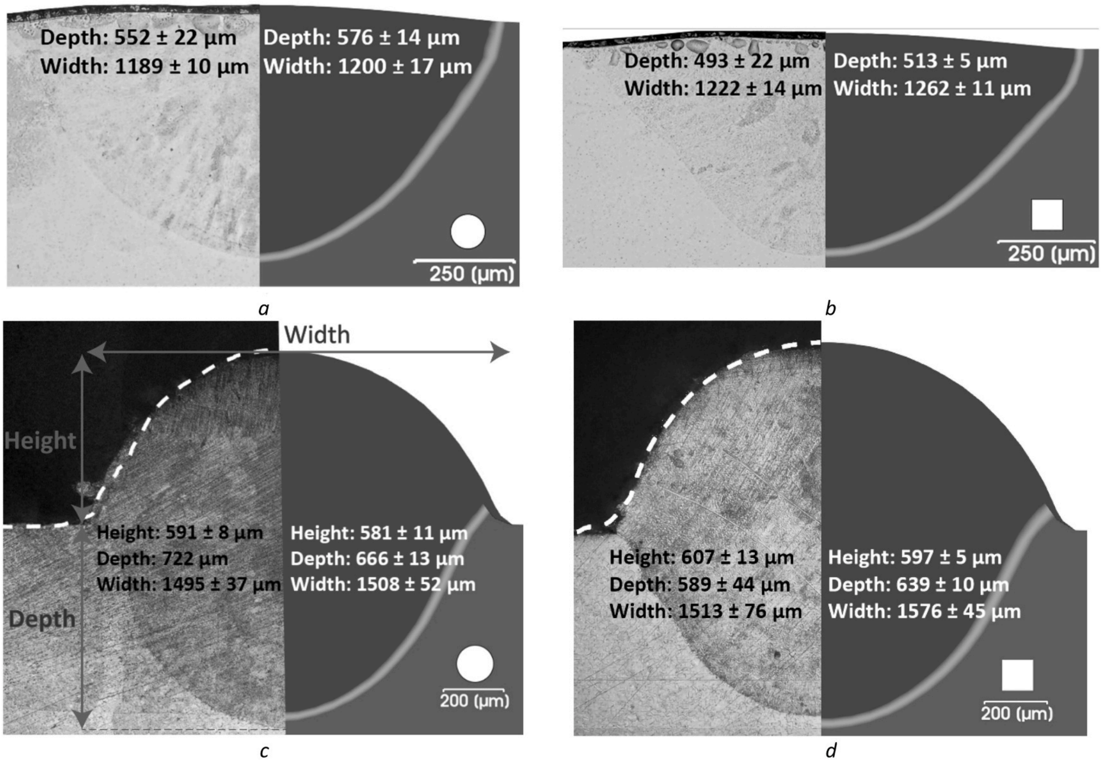

Fig. 2. Comparison between experimental (left) and numerical (right) transverse cross-sections of laser-melted tracks induced by (a) circular and (b) square-shaped intensity profiles at 700 W laser power and 20 mm s^{-1} scanning speed, and experimental and numerical cross-sections of single tracks generated by DED-LB with uniform (c) circular and (d) square intensity profiles, respectively, at 600 W laser power, 5 mm s^{-1} scanning speed, and 2.5 g min^{-1} powder feed rate. The laser spot shapes are shown beside the simulated melt pools. The white dashed curve represents the averaged height profile from multiple experimental cross-sections. All subfigures are adapted from Ref. [1].

2.2.1. Computational domain

The CA domain is discretized into uniformly spaced hexahedral unit volumes, referred to as cells in the following. Each cell is assigned a set of parameters, and the evolution of these parameters governs the resulting microstructure. These cell parameters encompass:

- center coordinates: $X(n_{CA})$,
- temperature: $T(n_{CA},\tau_{CA})$,
- metal fraction: $M(n_{CA},\tau_{CA})$,
- state (gas, liquid, growing, or solid): $I_s(n_{CA},\tau_{CA})$,
- grain index: $I_g(n_{CA},\tau_{CA})$,
- octahedron orientation as the grain crystallographic orientation: $O_g(n_{CA},\tau_{CA})$,
- center coordinates of the growing octahedron: $X_g(n_{CA},\tau_{CA})$, and
- octahedron size: $L_g(n_{CA},\tau_{CA})$.

Here, n_{CA} and τ_{CA} indicate the cell number and CA time-step, respectively. In the present CA model, a first-order Moore neighborhood is considered, which implies that each cell is surrounded by 26 neighboring cells [13,39]. Additionally, a fixed CA boundary condition is applied, implying that cells located on the boundary surfaces of the computational domain do not have any neighboring cells at their outer side(s) [38].

Fig. 3 shows a schematic of the CA computational domain. During the DED-LB process, the microstructure of the deposited layer(s) is formed upon the pre-existing microstructure of the substrate [11,17]. As an efficient approach in this study, in order to generate—i.e., to compute—the microstructure of the substrate, cells corresponding to the substrate are first identified based on the interpolated initial metal fraction of the thermal profile on the CA profile. The substrate is characterized as a region initially comprising solid metal cells, expressed as

$$n_{CA} \in substrate \mid I_s(n_{CA},\tau_{CA}=\tau_{th}=1)=solid\ state\ \&\ M(n_{CA},\tau_{CA}=\tau_{th}=1) \geq M_{cr}. \tag{1}$$

Here, M_{cr} denotes the critical metal fraction, set at 0.5 in this study; cells with $M \geq M_{cr}$ are treated as metal-filled, and those with $M < M_{cr}$ as gas. M_{cr} is a purely geometric threshold for binarizing the CA domain by mimicking the thermal free surface and does not influence grain growth physics. Next, the CA model is initially applied to the cells in the substrate to generate the microstructure of the substrate prior to laser processing. To do this, the initial temperature of the cells in the substrate is set to the liquidus temperature T_l, inducing a transition into a liquid state for these cells. Subsequently, the cells in the substrate are allowed to uniformly cool down until the cells reach a solid state. To mimic the actual microstructure of a substrate, nucleation-related parameters, specifically nucleation density and undercooling, are adjusted such that the average numerical grain size of the microstructure equals the average experimentally determined grain size in the (bulk of the) substrate.

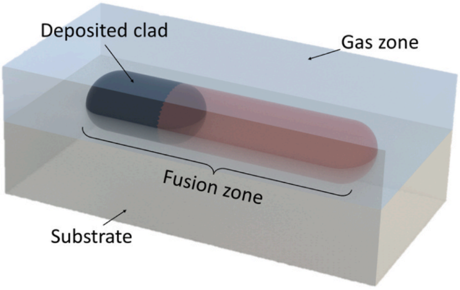

Fig. 3. Schematic representation of the Cellular Automata (CA) computational domain, consisting of cells in the substrate and fusion zone, but excluding cells in the gas zone. The cells in the fusion zone transition from a gas or solid state to a liquid state. Subsequently, these cells transition to a growing state and eventually into a solid state during the solidification of the material deposited.

The size of the CA computational domain follows from the domain size used in the thermal-fluid model and simulations. A sufficiently large CA domain is crucial to adequately capture the partial melting of grains in the substrate and facilitate the ongoing growth of grains. In the present study, a new algorithmic approach is used to determine and consider the minimum number of cells required for a sufficiently large CA domain. In the fusion zone, material undergoes a transition from an initial gas or solid state to a liquid state, followed by a growing state, and ultimately a solid state. Therefore, nodes in the fusion zone are in a liquid metal state at least once during the deposition process. The combination of nodes in the substrate and fusion zone assembles the point cloud of nodes, enclosing the largest required thermal domain size for the CA simulations. Subsequently, a so-called alpha shape [49,50], known for handling non-convex regions and potentially non-uniform thermal node distributions, is generated around the nodes located in the cloud. The cells located on or in this alpha shape (corresponding to the fusion zone in Fig. 3) constitute the CA computational domain, while the remaining cells consistently maintain a gas state and are thus logically excluded from the CA profile.

2.2.2. Coupling of thermal and microstructure profiles

In this study, a one-way weakly coupling scheme that maps the thermal field to the CA grid is utilized to reduce computational costs. In this approach, the simulation results from the thermal-fluid model serve as input for the microstructure model [44]. To that end, temperature and metal fraction values are interpolated into the CA grid. In this study, a computationally optimized interpolation method is proposed to increase the computational efficiency of the latter interpolation, which comprises the following sequential steps:

a) A Delaunay triangulation [51] instance is created from the thermal nodes, facilitating efficient queries on the thermal data.
b) For each cell in the CA model, the indices of the four nodes belonging to the tetrahedron enclosing the cell, as well as the Barycentric coordinates of the cell with respect to its enclosing nodal tetrahedron, are once determined and stored. Using the cell's Barycentric coordinates, $r = (r_1,r_2,r_3,r_4)$, and the property values at the nodes, $p = (p_1,p_2,p_3,p_4)$, the temperature and metal fraction values at each cell are interpolated from the enclosing four nodes using [52],

$$p_{cell} = r{\cdot}p = r_1p_1 + r_2p_2 + r_3p_3 + r_4p_4. \tag{2}$$

c) Once the CA time instance falls between two consecutive thermal time-steps, τ_{th} and $\tau_{th}+1$, the temperature and metal fraction values are interpolated from the thermal profile to the CA profile at the two thermal time-steps, resulting in $T(n_{CA},\tau_{th})$, $M(n_{CA},\tau_{th})$, $T(n_{CA},\tau_{th}+1)$, and $M(n_{CA},\tau_{th}+1)$.
d) The time ratio, denoted by α_t, is calculated as the fraction of time between the two thermal time-steps that has been covered by the current CA time. That is,

$$\alpha_t = \frac{t(\tau_{CA}) - t(\tau_{th})}{t(\tau_{th}+1) - t(\tau_{th})}. \tag{3}$$

e) Next, $Nt_1 = 1-\alpha_t$, and $Nt_2 = \alpha_t$ are calculated, which are the time fraction functions for CA time between thermal time-steps. Therefore, when $Nt_1 = 1$, and $Nt_2 = 0$, the CA time-step is equal to τ_{th}. Conversely, when $Nt_2 = 1$, and $Nt_1 = 0$, the CA time-step is equal to $\tau_{th}+1$.
f) To determine the temperature and metal fraction values at the current CA time between the two thermal time-steps (τ_{th} and $\tau_{th}+1$), a linear interpolation is employed, which is described by

$$T(n_{CA},\tau_{CA}) = T(n_{CA},\tau_{th}) \cdot Nt_1 + T(n_{CA},\tau_{th}+1)\cdot Nt_2, \tag{4}$$

$$M(n_{CA},\tau_{CA}) = M(n_{CA},\tau_{th}) \cdot Nt_1 + M(n_{CA},\tau_{th}+1)\cdot Nt_2. \tag{5}$$

Employing the above optimized interpolation technique, the properties of cells at the thermal time-steps, τ_{th} and $\tau_{th}+1$, are interpolated only once when the CA time falls within this interval. Then, as the CA time progresses within this thermal time interval, the properties are updated using a fast linear interpolation at the current CA time. This interpolation approach significantly reduces the computational cost compared to the direct thermal-to-CA property interpolation at every CA time-step, as shown by the dashed line in Fig. 4.

Once defining the CA domain, and the thermal-to-CA property interpolating the temperature and metal fraction at each CA time-step, grain nucleation and growth are tracked as detailed in the following subsections.

2.2.3. *Grain nucleation*

In the CA model, grain nucleation is based on a heterogeneous nucleation model, wherein the local undercooling of liquid cells is considered at the scale of dendrite arms [2,38]. This assumption reflects the dominance of interface-assisted nucleation in metal AM, where rapid solidification and limited time for bulk undercooling strongly favor nucleation at pre-existing interfaces [15,53]. Initially, a set of n_V cells in the CA domain are randomly selected as potential nucleation sites [2,38,53]. And n_V is calculated as,

$$n_V = N_V \cdot V_{CA}, \tag{6}$$

where V_{CA} is the volume of the CA domain, and N_V is the nucleation density. Next, a critical undercooling, ΔT_{cr}, is assigned to each potential nucleation site. The cell's undercooling, ΔT, is defined as the difference between the liquidus temperature and the current temperature of the cell, i.e., $\Delta T = T_l - T$. Critical undercooling is computed based on a normal distribution with a mean undercooling, ΔT_N, and a standard deviation undercooling, ΔT_σ. In cases where multiple critical undercoolings are assigned to a single site, the smaller value of the undercooling is selected [2,38]. It should be noted that a negative critical undercooling value indicates that nucleation occurs at a temperature higher than the liquidus temperature. To prevent this unphysical situation, as a physically consistent implementation in the present study, any negative critical undercooling value, ΔT_{cr}, sampled from the normal distribution is rejected and replaced by resampling from the same distribution until a positive value is obtained, thereby enforcing physical constraints while preserving the target mean and variance.

When the current undercooling, ΔT, of a potential nucleation site in a liquid metal state surpasses its critical undercooling, ΔT_{cr}, that site is labeled as an actual nucleation site or nucleus. Subsequently, the state of the cell is changed to the growing state, and a unique grain index is assigned to the cell [38]. Moreover, a regular octahedron is created, and its center coordinates are set to match those of the cell. The initial octahedron size at the nucleation instance is considered zero. The spatial orientation of this octahedron, as the crystallographic orientation, is determined based on three random Euler angles as a representation of the $Fm\overline{3}m$ crystallographic symmetry [2,54]. The six half-diagonals of the octahedron represent the <001> primary dendritic growth directions of the grain, while the octahedron is bounded by {111} planes [21,38,54]. Therefore, the CA model, employing octahedrons to represent dendritic growth, is suitable for simulating the solidification of metals with face-centered-cubic (FCC) and body-centered-cubic (BCC) crystal structures, given that their preferential growth direction is < 001> [2,21,54]. The material studied in this work is AISI 316L austenitic stainless steel, which features an FCC crystal structure.

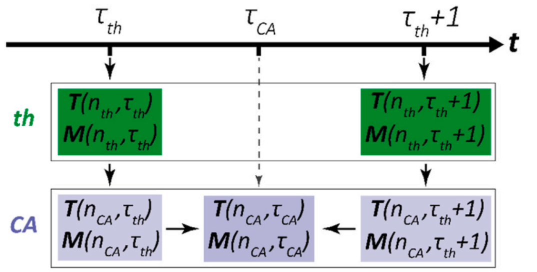

Fig. 4. Schematic representation of the proposed fast thermal-to-CA property interpolation method. First, the quantities T (temperature) and M (fluid fraction) are interpolated from the thermal (green) to the CA grid (purple) at the beginning of two sequential thermal time-steps (τ_{th} and $\tau_{th}+1$), respectively. Next, a linear interpolation is conducted for each CA time within this interval for the properties, resulting in significantly faster interpolation compared to the direct interpolation (dashed line) of properties from the thermal profile at each CA time.

2.2.4. *Grain growth*

The growth of the assigned octahedron in a growing cell is modeled by extending half-diagonals based on the dendrite tip velocity, v_{tip} [38]. This velocity, assumed as the grain growth velocity, is computed using a physically-based analytical model for dendrite kinetics [11], explained in more detail in Section 2.2.4.2. The dendrite tip velocity, v_{tip}, is updated at each CA time-step, based on the current undercooling at the center of the growing cells [40]. Assuming Δx as the cell size and Δt_{CA} as the current CA time-step size, the size of the octahedron, L_g, is defined as the normal distance from the octahedron center to one of its faces and is computed from the previous size, L_g^{old}, as [2,54],

$$L_g = L_g^{old} + \frac{v_{tip}\cdot\Delta t_{CA}}{\sqrt{3}}. \tag{7}$$

A rotation matrix, $\boldsymbol{R}_{ZXZ}$, is employed according to the grain crystallographic orientation to determine the coordinates of the vertices of the corresponding octahedron for each growing cell. The rotation sequence follows the ZXZ pattern, which is also known as the Bunge convention [55]. To compute the rotation matrix $\boldsymbol{R}_{ZXZ}$, Euler angles (φ_1, ϕ, φ_2) are used, where $\varphi_1, \varphi_2 \in [0, 2\pi]$ are the rotations around the Z-axis, and $\phi \in [0, \pi]$ is the rotation around the X-axis [55]. This matrix is a product of three individual rotation matrices, $\boldsymbol{R}_{Z,\varphi_1}$, $\boldsymbol{R}_{X,\phi}$, and $\boldsymbol{R}_{Z,\varphi_2}$ [55], and is defined as

$$\boldsymbol{R}_{ZXZ} = \boldsymbol{R}_{Z,\varphi_1}\boldsymbol{R}_{X,\phi}\boldsymbol{R}_{Z,\varphi_2} = \begin{bmatrix} cos(\varphi_1) & -sin(\varphi_1) & 0 \\ sin(\varphi_1) & cos(\varphi_1) & 0 \\ 0 & 0 & 1 \end{bmatrix} \begin{bmatrix} 1 & 0 & 0 \\ 0 & cos(\phi) & -sin(\phi) \\ 0 & sin(\phi) & cos(\phi) \end{bmatrix} \begin{bmatrix} cos(\varphi_2) & -sin(\varphi_2) & 0 \\ sin(\varphi_2) & cos(\varphi_2) & 0 \\ 0 & 0 & 1 \end{bmatrix}. \tag{8}$$

Accordingly, the coordinates of the octahedron vertices assigned to each growing cell follow from

$$\boldsymbol{OV} = \sqrt{3}\cdot L_g \cdot \left(\boldsymbol{R}_{ZXZ} \times \boldsymbol{OV}_{unit}{}^{T}\right)^{T} + \boldsymbol{OC}, \tag{9}$$

where $\boldsymbol{OV}$ is a 6 × 3 matrix containing the new coordinates of the six octahedron vertices, and $\boldsymbol{OC}$ is a 6 × 3 coordinates matrix compatible with the cross operator. The latter comprises the repeated center coordinates of the corresponding grain, which is denoted as X_g. The matrix $\boldsymbol{OV}_{unit}$ contains the coordinates of the vertices of a unit octahedron, given by,

$$\boldsymbol{OV}_{unit} = \begin{bmatrix} 1 & 0 & 0 \\ -1 & 0 & 0 \\ 0 & 1 & 0 \\ 0 & -1 & 0 \\ 0 & 0 & 1 \\ 0 & 0 & -1 \end{bmatrix}. \tag{10}$$

Of each growing cell, the centers of neighboring undercooled liquid metal cells are examined to determine whether the neighboring cell is “captured” by the growing octahedron of the growing cell [54]. When the octahedron of the growing cell captures the center of a neighboring undercooled liquid metal cell, the state of the captured cell is reassigned from a liquid state to a growing state. Subsequently, the captured cell is assigned the same grain index as the capturing cell, and a new octahedron is defined in the captured cell, preserving the same crystallographic orientation as the capturing cell [54]. However, the center coordinates and size of this new octahedron are determined using the “decentered octahedron algorithm” [54], as explained in more detail in Section 2.2.4.2. When multiple octahedrons capture the same cell, one of these octahedrons triggers the formation of a larger octahedron within the captured cell. In this case, the characteristics of the cell associated with this capturing octahedron are subsequently assigned to the captured cell. When the state of all neighboring cells of a growing cell is either a solid or growing state, the state of the growing cell transitions to a solid state, signifying the completion of the growth process of the cell.

When the temperature of a solid or growing cell surpasses the liquidus temperature, the cell undergoes a transition to the liquid state, resetting its microstructure data (no grain index, no octahedron center, length, and crystallographic orientation) [17,20]. Also, in this case, the state of the solid cells in the neighborhood of the liquid cell changes from a solid to a growing state, forming a layer of growing cells between the solid and liquid cells [13,56]. In addition to excluding the always remaining gas cells from the CA domain, during DED-LB, certain liquid or solid cells may be subject to evaporation or free surface movement, leading to the condition that the metal fraction of the cell is smaller than the critical metal fraction—i.e., $M(n_{CA}, \tau_{CA}) \leq M_{cr}$. In the latter case, as an efficient implementation in the present research, the state of the cells undergoes a change to the gas state, accompanied by a reset of their microstructure data. In addition, at each CA time-step, the grain nucleation and growth conditions are applied only if at least one liquid or growing metal cell exists. Otherwise, the current CA time-step is disregarded, and the CA simulation progresses to the subsequent CA time-step. This approach assures that only relevant cells are examined, thereby increasing the computational efficiency of the simulation.

2.2.4.1. Dendrite growth kinetics. In the early 1980s, the need to predict microstructure evolution during rapid solidification drove the development of analytical models for free dendritic growth. These models were formulated to provide a more accurate description of the growth of dendrites in undercooled melts and to calculate the dendrite tip radius and velocity as a function of the undercooling components. Among the most well-known analytical models [57–59], the Boettinger-Coriell-Trivedi (BCT) model [57] was the first effort to accurately address non-equilibrium solute partitioning at the solid-liquid interface in a free dendritic growth model [58]. While using the Aziz solute trapping model [60] and the Trivedi-Kurz stability criterion [61], it adheres to the thermodynamic requirement that the compositions at the solid-liquid interface fall within a range that generates a positive interfacial driving force. Moreover, the BCT model satisfies the kinetic requirement that the interface migrates at a rate proportional to the attachment rate of atoms to the growing solid, which may be proportional to the interfacial driving force at relatively low undercooling. By incorporating the interfacial driving force, the BCT model correctly defines total undercooling, incorporating four undercooling components, namely thermal (ΔT_T), compositional (ΔT_C), curvature (ΔT_R), and kinetic (ΔT_K) undercoolings [58].

To calculate the dendrite tip velocity that serves as the grain growth velocity in the CA model, the BCT model [57] is used in the present study. The total undercooling of the melt can be expressed as,

$$\begin{aligned} \Delta T = T_l(C_0) - T = \Delta T_T + \Delta T_C + \Delta T_R + \Delta T_K = \frac{\Delta H_f}{c_p} \cdot I_v(P_t) \\ + m_e \cdot C_0 \left[1 - \frac{\frac{m}{m_e}}{1 - (1-k) \cdot I_v(P_c)} \right] + \frac{2\Gamma}{r_{tip}} + \frac{v_{tip}}{\mu_K}, \end{aligned} \tag{11}$$

where ΔH_f is the enthalpy of fusion per unit mass, c_p is the specific heat, m_e denotes the slope of the equilibrium liquidus, C_0 represents the nominal concentration of solute in the melt, Γ is the Gibbs–Thompson coefficient—i.e., the interface energy/entropy of fusion [15,42,44], μ_K represents the kinetic interface coefficient and v_{tip} and r_{tip} are the dendrite tip velocity and radius, respectively. Further, $I_v(P)$ is the Ivantsov function that addresses the coupled heat and mass transport around a paraboloidal dendrite tip in steady-state free dendritic growth [11],

$$I_v(P) = P \cdot \exp(P) \cdot E_1(P), \tag{12}$$

where $E_1(P)$ is the exponential integral function of the first kind [15],

$$E_1(P) = \int_P^{\infty} \frac{\exp(-t)}{t} dt, \tag{13}$$

and P_t and P_c are the thermal and solute Peclet numbers, respectively [11,15,42],

$$P_t = \frac{v_{tip} \cdot r_{tip}}{2\alpha}, \tag{14}$$

$$P_c = \frac{v_{tip} \cdot r_{tip}}{2D_l}, \tag{15}$$

where D_l is chemical diffusivity in the liquid phase, and α is the thermal diffusivity of the supercooled liquid. Further, k is the kinetic partition coefficient [62],

$$k = \frac{C_s^*}{C_l^*} = \frac{k_e + \frac{v_{tip}}{v_D}}{1 + \frac{v_{tip}}{v_D}}. \tag{16}$$

Here, the superscript * indicates the solid-liquid interface. Further, k_e is the equilibrium partition coefficient, v_D is the solute trapping velocity as D_l/a [63], where a is the interatomic spacing or lattice parameter. Further, m is the kinetic liquidus slope defined as [62],

$$m = m_e \left[\frac{1 - k\left(1 - ln\frac{k}{k_e}\right)}{1 - k_e} \right]. \tag{17}$$

As a supplementary equation, the Trivedi-Kurz stability criterion [61] is needed to describe the non-equilibrium interfacial kinetics that arise during rapid solidification in the context of free dendritic growth under equal thermal diffusivity and conductivity in the solid and liquid phases [61]. The criterion is formulated as,

$$r_{tip} = \frac{\frac{\Gamma}{\sigma^*}}{\frac{P_t \cdot \Delta H}{c_p} \xi_t - \frac{2m_e \cdot P_c \cdot C_0 (1-k)}{1-(1-k) \cdot I_v(P_c)} \xi_c}, \tag{18}$$

where σ^* is the stability parameter ($\approx \frac{1}{4\pi^2}$). ξ_t and ξ_c are the thermal and solute stability parameters, respectively, which are defined as [57],

$$\xi_t = 1 - \frac{1}{\sqrt{1 + \frac{1}{\sigma^* \cdot P_t^2}}}, \tag{19}$$

$$\xi_c = 1 + \frac{2k}{1 - 2k - \sqrt{1 + \frac{1}{\sigma^* \cdot P_c^2}}}. \tag{20}$$

The properties of 316L austenitic stainless steel employed in the BCT model are listed in Table 1.

Fig. 5 shows the dendrite tip velocity as a function of undercooling determined by the BCT model and material parameters, used in the present study. Rather than resolving the BCT model for each undercooling corresponding to individual growing cells, a common approach involves initially determining the dendrite tip growth velocity across a broad range of undercoolings and then fitting an exponential or polynomial function [11,40,54]. However, given the multiple changes in the curvature of the dendrite tip velocity versus undercooling curve (Fig. 5), a more accurate approach to capture the curve's variations is linear interpolation on a data table of the dendrite tip velocity at specific undercoolings.

2.2.4.2. Decentered octahedron algorithm. In this study, the center coordinates and size of an octahedron within a captured cell are determined using the so-called “decentered octahedron algorithm” [54]. This algorithm was originally introduced by Gandin and Rappaz [54], and is adapted here. The latter approach mitigates the artificial anisotropy caused by neighborhood type, cell type, or grid orientation. In this approach, a growing octahedron, characterized by its center coordinates C_μ, is associated with a growing cell, μ, whose center coordinates are designated as X_μ. When this octahedron captures the center of a neighboring cell, ν, characterized by the center coordinates X_ν, a new octahedron with the center coordinates C_ν and the initial size of L_ν is defined in the cell ν. As shown in Fig. 6 (print) or Video 1 (online), the new octahedron always fits within the capturing octahedron.

The determination of the center coordinates, C_ν, and initial size, L_ν, of the new octahedron involves carrying out the following steps [2,38,48,54]:

a) The three nearest vertices of the growing octahedron, namely S_1, S_2, and S_3 are determined and subsequently sorted in order of their distance to the cell center coordinates, X_ν,

b) the normal unit vector of the plane formed by S_1, S_2, and S_3 is determined from

$$\overrightarrow{n_s} = \frac{\left(\overrightarrow{S_2 - S_1}\right) \times \left(\overrightarrow{S_3 - S_1}\right)}{\left\| \left(\overrightarrow{S_2 - S_1}\right) \times \left(\overrightarrow{S_3 - S_1}\right) \right\|}, \tag{21}$$

c) the projected point, P_ν, from the coordinates X_ν onto the plane $\overline{S_1 S_2 S_3}$ is determined from

$$P_\nu = X_\nu - \left[\left(\overrightarrow{X_\nu - S_1}\right) \cdot \overrightarrow{n_s}\right] \overrightarrow{n_s}, \tag{22}$$

Table 1
Properties of the 316L austenite stainless steel used in the BCT model.

Property	Value	Unit	Source
T_s	1637	K	[1]
T_l	1715	K	[1]
ΔH_f	$2.6 \cdot 10^5$	$\mathrm{J \cdot kg^{-1}}$	[1]
c_p	778	$\mathrm{J \cdot kg^{-1} \cdot K^{-1}}$	[64]
Γ	$3.47 \cdot 10^{-7}$	$\mathrm{K \cdot m}$	[65]
C_0	17	wt%	[65–67]
k_e	0.791	-	[65]
μ_K	0.6489	$\mathrm{m \cdot s^{-1} \cdot K^{-1}}$	[68]
D_l	$3 \cdot 10^{-9}$	$\mathrm{m^2 \cdot s^{-1}}$	[19,65]
a	$3.67 \cdot 10^{-10}$	m	[69]
m_e	-3.49	$\mathrm{K \cdot wt\%^{-1}}$	[65]
ρ	6988	$\mathrm{kg \cdot m^{-3}}$	[1]
k_{th}	29	$\mathrm{W \cdot m^{-1} \cdot K^{-1}}$	[1]

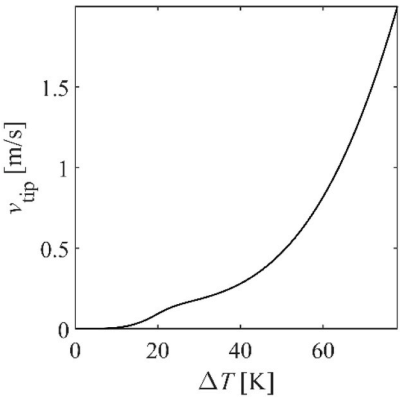

Fig. 5. The calculated dendrite tip velocity, v_{tip}, as a function of undercooling ΔT using the BCT model.

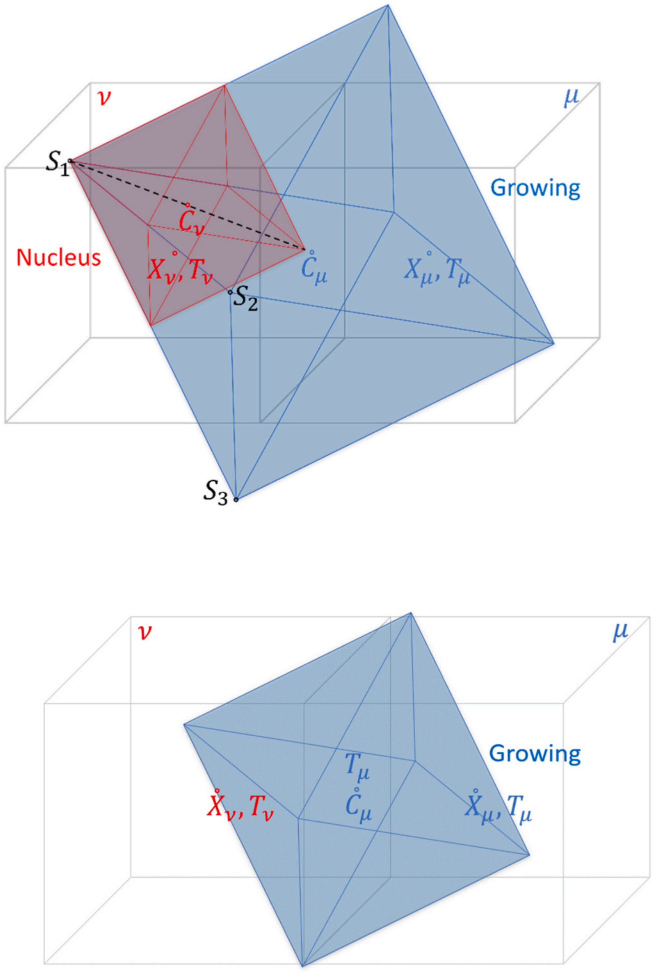

Fig. 6. (print)/Video 1 (online): Decentered octahedron algorithm. As the octahedron of the growing cell (μ), shown in blue, captures the center (C_ν) of a neighboring undercooled liquid metal cell (ν), a new octahedron, shown in red, is generated in ν with calculated center coordinates, C_ν, and initial size, L_ν, inheriting the orientation of the capturing octahedron. The growth rate of each octahedron depends on the undercooling at the center of its corresponding cell. Growth stops once all neighboring cells transition from the liquid state, indicating solidification.

d) the projected point I from P_ν to the edge $\overline{S_1S_2}$ and the projected point J, from P_ν to the edge $\overline{S_1S_3}$ are determined from

$$I = S_1 + \frac{\left(\overrightarrow{P_\nu - S_1}\right)\cdot\left(\overrightarrow{S_2 - S_1}\right)}{\left(\overrightarrow{S_2 - S_1}\right)\cdot\left(\overrightarrow{S_2 - S_1}\right)}\left(\overrightarrow{S_2 - S_1}\right), \tag{23}$$

$$J = S_1 + \frac{\left(\overrightarrow{P_\nu - S_1}\right)\cdot\left(\overrightarrow{S_3 - S_1}\right)}{\left(\overrightarrow{S_3 - S_1}\right)\cdot\left(\overrightarrow{S_3 - S_1}\right)}\left(\overrightarrow{S_3 - S_1}\right), \tag{24}$$

e) the size of the new octahedron, L_ν, is determined as follows

$$L_\nu = \sqrt{2/3}\,max(L_{12}, L_{13}), \tag{25}$$

where, the lengths L_{12} and L_{13} are determined from

$$L_{12} = \frac{1}{2}\left[\min\left(\left\|\overrightarrow{S_1 - I}\right\|, \sqrt{3}\,\Delta x\right) + \min\left(\left\|\overrightarrow{S_2 - I}\right\|, \sqrt{3}\,\Delta x\right)\right], \tag{26}$$

$$L_{13} = \frac{1}{2}\left[\min\left(\left\|\overrightarrow{S_1 - J}\right\|, \sqrt{3}\,\Delta x\right) + \min\left(\left\|\overrightarrow{S_3 - J}\right\|, \sqrt{3}\,\Delta x\right)\right]. \tag{27}$$

If the lengths of $\overrightarrow{IS_1}$, $\overrightarrow{IS_2}$, $\overrightarrow{JS_1}$, and $\overrightarrow{JS_2}$ are all smaller than $\sqrt{3}\Delta x$ (maximum spacing between neighboring cell centers), then the new octahedron has the same size as the capturing octahedron.

f) Finally, the center coordinates of the new octahedron, C_ν, is determined from,

$$C_\nu = S_1 + \sqrt{3}L_\nu \cdot \frac{C_\mu - S_1}{\left\|\overrightarrow{C_\mu - S_1}\right\|}. \tag{28}$$

2.2.5. *Enhancing memory efficiency and accelerating computation*

In the previous sections, various strategies, including CA domain size optimization and fast thermal-to-CA property interpolation, were presented to enhance the performance of the CA model. Additionally, this section presents further techniques designed for this purpose without altering the underlying physics or introducing any simplifications to the governing model.

2.2.5.1. Spatial pre-processing of thermal profile. In order to reduce the computation cost, a novel algorithmic approach is presented in this section to further exclude several nodes from the thermal profile before interpolating the properties to the CA profile. To that end, three cases can be considered. First, before determining the size of the CA domain, nodes associated with the gas region (see Fig. 3) are identified as those regions consistently having a zero metal fraction throughout all thermal time-steps. Therefore, as solidification occurs within the metal region, gas nodes and their associated data can be, and are, excluded from the thermal profile. Secondly, it is possible to exclude the metal nodes with a temperature history consistently below a specific temperature, e.g., the solidus temperature, in the case that the complete geometry of the substrate is not of interest for consideration in the microstructure simulation. Thirdly, after defining the size of the CA domain, but before the grain nucleation and growth processes, the union of the 27 nearest nodes for each cell is identified. The latter forms a node cloud as the smallest required thermal domain enclosing the CA domain. The remaining nodes—i.e., outside the smallest thermal domain enclosing the CA domain, and their associated thermal data are removed from the thermal profile.

2.2.5.2. Temporal pre-processing of thermal profile. Similar to what was discussed in Section 2.2.5.1, the thermal profile can be shrunk in terms of time. Accordingly, thermal time-steps during which solidification does not occur are excluded. This novel algorithmic approach is explained here.

Step 1 Define the nucleation temperature range

When the temperature of the liquid metal cell with the lowest temperature drops within the range suitable for nucleation during the cooling phase of the cell, the first nucleation event may occur, thereby activating the microstructure model. The temperature range in which nucleation occurs, as shown in Fig. 7, is described by

$$T_{nuc,min} = T_l - max(\Delta T_N) - 4\,max(\Delta T_\sigma) < T < T_l - min(\Delta T_N) + 4\,max(\Delta T_\sigma) = T_{nuc,max}, \tag{29}$$

where $T_{nuc,min}$ and $T_{nuc,max}$ are the minimum and maximum temperatures at which a nucleation event can take place.

Step 2 Account for material variations

In cases where the powder and substrate material are not the same or in cases where the nucleation behavior is different across multiple regions (Fig. 3), multiple sets of mean and standard deviation undercoolings may be used. As shown in Fig. 7:

- To determine $T_{nuc,min}$ as the minimum temperature at which nucleation may occur, the largest value among the mean undercooling ΔT_N values and the largest value among the standard deviation undercooling ΔT_σ values are considered.
- To determine $T_{nuc,max}$, as the closest temperature to the liquidus temperature, the smallest value of the mean undercooling ΔT_N and the largest value among the standard deviation undercooling ΔT_σ values are taken into account.

Step 3: Identify the solidification time window

In CA modeling of DED-LB, the focus is on the thermal time range where solidification occurs, while disregarding thermal data associated with the remaining thermal time ranges. The start of the solidification time window is identified and modified as follows,

a) Nodes are identified that first undergo a metal liquid state exposed to a temperature exceeding the liquidus temperature, and later a metal state with a temperature lower than the maximum temperature $T_{nuc,max}$ at which a nucleation event can occur.
b) For each such node, the earliest time-step at which the metal node cools down below $T_{nuc,max}$ is determined.
c) The earliest time-step among these identified time-steps is found.
d) The time-step immediately preceding this earliest time-step is designated as the modified first time-step.

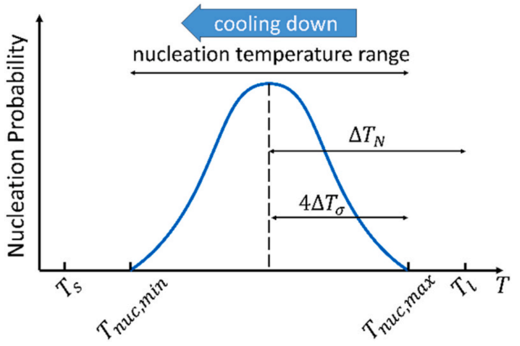

Fig. 7. Schematic representation of the nucleation temperature range in the CA model. The nucleation probability is assumed as a normal distribution with mean and standard deviation undercoolings of ΔT_N and ΔT_σ, respectively.

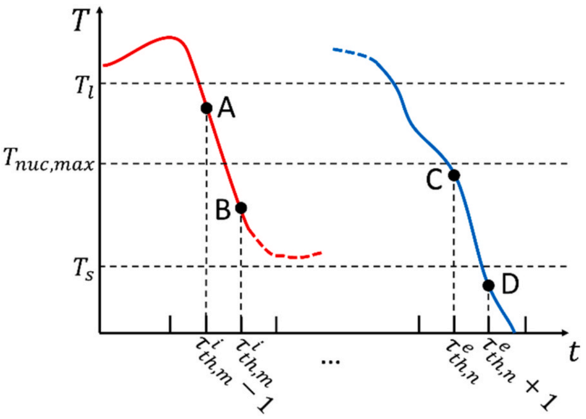

Fig. 8. Schematic representation of the minimum required thermal time range (from $\tau^i_{th,m} - 1$ to $\tau^e_{th,n} + 1$) for the simulation of the solidification process. The red curve on the left side represents the temperature variation of the first node experiencing solidification, while the blue curve on the right side represents that of the last node. The first nucleation event occurs at a moment between $\tau^i_{th,m} - 1$ and $\tau^i_{th,m}$, and the last solidification event happens between $\tau^e_{th,n}$ and $\tau^e_{th,n} + 1$.

e) All time-steps prior to this modified first time-step and their corresponding nodal data are removed from the thermal profile.

Assuming the red curve shown on the left side in Fig. 8 as the schematic representation of the temporal temperature change of a metal node experiencing cooling to point B below $T_{nuc,max}$ at time-step $\tau^i_{th,m}$ sooner than other nodes, the modified first time-step is $\tau^i_{th,m} - 1$.

Similarly, the end of the solidification time window is identified and modified as follows,

a) The latest thermal time-step where the temperature of at least one metal node is higher than the solidus temperature is identified as $\tau^e_{th,n}$.
b) The time-step following this time-step, $\tau^e_{th,n} + 1$, is considered the modified last time-step.
c) All time-steps and related nodal data after this modified last time-step are also removed from the thermal profile.

The blue curve on the right side of Fig. 8 schematically represents the temporal temperature change of the last metal node experiencing the temperature at point C above the solidus temperature at $\tau^e_{th,n}$. Accordingly, the modified last time-step is $\tau^e_{th,n} + 1$.

2.2.5.3. Spatial pre-processing of CA profile. The CA model can be more efficient by confining the growth process (Section 2.2.4) to cells within the fusion zone only. More specifically, the latter cells are positioned in a zone limited by the inclusion of fusion nodes and their 27 neighboring nodes. This method guarantees that no fusion zone cell surpasses the thermal fusion zone boundaries, presenting an efficient application of the CA model exclusively to the pertinent cells.

2.2.5.4. Temporal pre-processing of CA profile. When the CA time-step size is smaller than the thermal time-step size, the initial CA time-step can have a forward jump compared to the first thermal time-step to expedite the calculation time, based on a new approach presented as follows. To achieve this, the metal nodes with a temperature higher than $T_{nuc,min}$ are denoted as $n_{th,nuc}$ at each thermal time-step. The maximum cooling rate among the cooling rates belonging to $n_{th,nuc}$ nodes at each thermal time-step is determined as,

$$\dot{T}_{max,\tau_{th}} = \max\left[\frac{T(n_{th,nuc},\tau_{th}) - T(n_{th,nuc},\tau_{th}+1)}{t(\tau_{th}+1) - t(\tau_{th})}\right] > 0. \tag{30}$$

Following this, the thermal time-step $\tau_{th,nuc1}$, at which the first nucleation event can potentially take place, is identified based on the condition that at its subsequent thermal time-step, $\tau_{th,nuc1} + 1$, the temperature of at least one node among the $n_{th,nuc}$ nodes falls below the minimum temperature of nucleation $T_{nuc,min}$. Nodes satisfying this condition are denoted as $n_{th,nuc1}$. The time-step size $\Delta t_{CA,jump}$ required for the first CA time-step to deviate from the first thermal time-step can be determined from,

$$\begin{aligned}\Delta t_{CA,jump} = \min\Big\{ & t(\tau_{th,nuc1}+1) - \left[t(\tau_{th,nuc1}+1) - t(\tau_{th,nuc1})\right] \\ & \cdot \frac{T(n_{th,nuc1},\tau_{th,nuc1}+1) - T_{nuc,min}}{T(n_{th,nuc1},\tau_{th,nuc1}+1) - T(n_{th,nuc1},\tau_{th,nuc1})}\Big\} \geq 0.\end{aligned} \tag{31}$$

2.2.5.5. CPU acceleration. The computational efficiency of the CA model is significantly enhanced through a novel parallelization strategy implemented for the grain growth algorithm. The most computationally intensive component of the model involves determining whether neighboring liquid metal cells are captured by the octahedra associated with growing cells and subsequently establishing new octahedra within the captured cells. This process traditionally requires nested for-loops: an outer loop iterating over all growing cells and an inner loop examining the captured cells for each growing cell. The primary challenge in parallelizing such nested loops lies in managing data dependencies between iterations. In the present study, a sophisticated parallel algorithm, as presented below, has been developed that effectively eliminates these dependencies while maintaining computational accuracy. The CPU parallelization strategy employs a three-phase approach: (1) Data preparation where all read-only variables are broadcast to workers as constants; (2) Parallel grain growth computation where each worker independently processes assigned growing cells, storing captured-cell records in thread-local lists without synchronization; and (3) Conflict resolution where globally captured records are merged and the octahedron producing the largest size is assigned to each captured cell.

2.2.5.5.1. Phase 1: Data preparation and parallelization constants. Prior to parallel execution, all variables that remain constant during the parallel computation are converted to parallelization constants. This approach ensures that these variables are copied to workers only once, rather than at each iteration, thereby minimizing memory transfer overhead. The key parallelization constants include:

- $Coords = \{coords_1, \ldots, coords_{N_{cells}}\}$, where $coords_i \in \mathbb{R}^3$ is the cell-center coordinates, and N_{cells} is the number of the cells,
- $UnitVertices = \{unitVertex_1, \ldots, unitVertex_6\}$, where $unitVertex_k \in \mathbb{R}^3$ is the vertex coordinates of the unit octahedron,
- $GrowCells = \{growCell_1, \ldots, growCell_{N_{growing\ cells}}\} \subseteq \{1, \ldots, N_{cells}\}$: Set of the indices of all growing cells, where $N_{growing\ cells}$ is the number of the growing cells,
- For each $growCell_i \in GrowCells$:
  - $LiqNeigs_i = \{liqNeig_{i,1}, \ldots, liqNeig_{i,N_j}\}$: Indices of liquid-metal neighbors of $growCell_i$, where $N_j \leq 26$ is the number of these neighbors,
  - $CoolLiqNeigs_i = \{coolLiqNeig_{i,1}, \ldots, coolLiqNeig_{i,N_k}\}$: Indices of supercooled-liquid-metal neighbors of $growCell_i$, where $N_k \leq N_j$ is the number of these supercooled neighbors,
  - $\boldsymbol{R}_{ZXZ,i} \in \mathbb{R}^{3\times 3}$: Rotation matrix based on the crystallographic Euler angles of $growCell_i$,
  - $octaLen_i$: Octahedron length of $growCell_i$,
  - $octaCenter_i \in \mathbb{R}^3$: Global center coordinates of the octahedron in $growCell_i$.

2.2.5.5.2. Phase 2: parallel computation. The core parallelization strategy employs a list of objects to store the captured cell information independently for each growing cell. The parallel computation proceeds as follows, where each worker independently processes its assigned growing cells. This design ensures thread-safe execution without race conditions.

Let each parallel task work on a single $growCell_i \in GrowCells$ and records the capture results in $captureRec_i$ as a (initially empty) local list of capture records for $growCell_i$:

a) Fetch supercooled neighbors
- If $CoolLiqNeigs_i$ is empty, go to Step “d”.

b) Construct a rotated octahedron
- Compute the six vertices of an octahedron of size $octaLen_i$, centered at $octaCenter_i$, rotated by $\boldsymbol{R}_{ZXZ,i}$: $OctaVertices_i = \left\{octaCenter_i + \sqrt{3} \times octaLen_i \times \boldsymbol{R}_{ZXZ,i} \times unitVertex_k \middle| unitVertex_k \in UnitVertices\right\}$.
- Form the minimal closed shape (α-shape) enclosing $OctaVertices_i$. Its volume should not be zero.

c) Identify and process capturable neighbors
- Compute $CapturedNeigs_i = \left\{coolLiqNeig_{i,j} \in CoolLiqNeigs_i \middle| coords_{coolLiqNeig_{i,j}} \textit{ lies inside the } \alpha\text{-shape}\right\}$.
- If $CapturedNeigs_i$ is empty, skip the current $growCell_i$; otherwise, for each $capturedNeig_j \in CapturedNeigs_i$:
  - o Apply the decentered-octahedron subroutine with inputs ($Coords$, $octaLen_i$, $OctaVertices_i$, $octaCenter_i$, $capturedNeig_j$) to obtain ($octaLen_{i,j}$, $octaCenter_{i,j}$): the length and center coordinates of the new octahedron in $capturedNeig_j$ induced by the octahedron of $growCell_i$.
  - o Append the record ($growCell_i$, $capturedNeig_j$, $octaLen_{i,j}$, $octaCenter_{i,j}$) to $captureRec_i$.

d) Solidification check
- If $LiqNeigs_i$ and $CoolLiqNeigs_i$ are empty, mark $growCell_i$ as “solidified”.

e) Return
- Output the local list $captureRec_i$.

2.2.5.5.3. Phase 3: Conflict resolution and state update. After parallel execution is completed, all local lists are merged into a single list. A critical aspect of the algorithm involves resolving conflicts when multiple growing cells attempt to capture the same undercooled liquid metal cell. The algorithm implements a maximum octahedron length criterion: when multiple octahedra overlap a liquid cell, the cell is assigned to the growing cell that creates the largest octahedron within it. This is achieved through:

a) Flatten capture records
- Let $CaptureRec = \bigcup_{i=1}^{M} captureRec_i = \{(capturingCells, capturedCells, octaLens, octaCenters)\}$.

b) Group by captured cell
- For each unique captured cell $capturedCell_k \in capturedCells$, collect all records $\left\{\left(capturingCells_k, capturedCell_k, octaLens_k, octaCenters_k\right)\right\} \subseteq CaptureRec$.

c) Select maximum-length assignment and update variables
- For each $capturedCell_k$
  - o Choose the record $\left(capturingCell_k^*, capturedCell_k, octaLen_k^*, octaCenter_k^*\right)$ for which $octaLen_k^* = \max\{octaLens_k\}$.
  - o Discard all other records for that $capturedCell_k$.
  - o Change the state of $capturedCell_k$ from “liquid” to “growing”.
  - o Update the grain index and crystallographic Euler angles of $capturedCell_k$ to those of $capturingCell_k^*$.
  - o Update the length and center coordinates of the octahedron in $capturedCell_k$ to $octaLen_k^*$ and $octaCenter_k^*$, respectively.

d) Update solidified cells
- For each cell marked “solidified” in Phase 2, update its state to “solid”.

Several optimization strategies are incorporated in the proposed algorithm to enhance computational efficiency. Memory efficiency is achieved through the use of parallelization constants, which minimizes memory duplication across workers for the large, read-only data structures. Load balancing is handled by the parallel for loop, which distributes iterations among available workers for optimal CPU utilization. Communication overhead is minimized through the list-of-objects approach, which eliminates the need for inter-worker data exchange during parallel execution. Furthermore, computational efficiency within each worker is maximized through the use of vectorized operations wherever applicable.

2.2.6. *Time-step size*

In the present study, the calculation of the new time-step size in the current CA model comprehensively takes several factors into account. First, to prevent a large CA time-step size causing the CA time to exceed the last thermal time, the upper limit for the CA time-step size is updated at each CA iteration as,

$$\Delta t_{max,1} = t_{th,last} - t_{CA}. \tag{32}$$

where $t_{th,last}$ is the total thermal time, and t_{CA} is the current CA time. Furthermore, if at the current time-step there exist actual nucleation sites fulfilling the conditions in Section 2.2.3, the time-step size should remain sufficiently small to facilitate a gradual temperature decrease, allowing for the nucleation event to occur at the appropriate temperature (see Fig. 7).

$$\Delta t_{max,2} = \frac{\min(\Delta T_\sigma)}{\dot{T}_{max,\tau_{th}}} \textit{ if nuclei; else}\infty, \tag{33}$$

In Addition, in laser processing, the CA time-step size should be small enough to prevent the propagation of the growth front and diffusion of the quantities over a distance longer than the cell size

$$\Delta t_{max,3} = \frac{\Delta x}{4 v_l}, \tag{34}$$

$$\Delta t_{max,4} = \frac{\Delta x^2}{4 D_l}, \tag{35}$$

In laser material processing, the velocity, v, corresponds to the laser beam scanning velocity, v_l, while in processes like casting, where the solidification front velocity is unpredictable based on the process parameters, v represents the maximum dendrite tip velocity, denoted as $v_{tip,max}$, for the growing cells.

Accordingly, the equation to determine the new time-step size is modified to,

$$\Delta t_{max} = \min\left(\Delta t_{max,1}, \Delta t_{max,2}, \Delta t_{max,3}, \Delta t_{max,4}\right), \tag{36}$$

If there is no growing cell at a CA time-step, the maximum dendrite tip velocity at that time-step is zero. In this case, the new time is updated by Ref. [70],

$$\Delta t = \min\left[\Delta t_{max}, \frac{\rho \cdot c_p \cdot \Delta x^2}{6 k_{th}}\right], \tag{37}$$

Otherwise,

$$\Delta t = \Delta t_{max}. \tag{38}$$

3. Experimental setup and procedures

The experimental setup for the DED-LB process consists of a Yb:YAG disk laser source (TruDisk 10001, TRUMPF SE + Co. KG, Germany) emitting a laser beam at a wavelength of 1030 nm. The laser system is equipped with optical transport fibers and focusing optics (BEO D70, TRUMPF SE + Co. KG, Germany) that deliver laser beams perpendicularly to the substrate's surface. The focusing optics are mounted to the end-effector of a 6-DOF robot (IRB-2600M2004, ABB AG, Sweden). 316L stainless-steel powder (median particle size d50 = [value] μm) is delivered from a Twin-150 powder feeder (Oerlikon Metco AG, Switzerland) to the laser-induced melt pool in the substrate through an off-axis powder nozzle (Fraunhofer ILT, Germany) with a 1.5 mm inner diameter. The powder is injected into the melt pool at a 70° angle to the horizon. Argon gas is used as both the transport gas and the shielding gas, flowing at rates of 2.5 NLPM (normal liter per minute) and 20 NLPM, respectively. The melt pool is shielded from oxidation by an additional nozzle (Fraunhofer ILT, Germany) that supplies argon. The laser beam intensity profiles are generated using different transport fibers. A 600 μm circular core fiber generates a circular uniform intensity profile, while a 620 × 620 μm^2 square core fiber generates a square uniform beam shape. The fiber exit is followed by a collimating lens with a 200 mm focal length, and then the beam is focused using a 400 mm focal length lens. This results in a uniform circular intensity profile with a diameter of 1.2 mm and a square intensity profile with dimensions of 1.24 × 1.24 mm^2. Fig. 9 shows measurements of these two profiles, published in our previous works [1,16,71,72].

During the deposition process, single tracks are deposited by the 316L stainless steel powder particles on a substrate of the same material. The tracks are deposited at a velocity of 5 mm/s at a laser power of 600 W and a powder flow rate of 2.5 g/min. In the laser melting process (no supply of powder), a laser power of 700 W and a scanning velocity of 20 mm/s are used [16,71].

The deposited tracks are analyzed from the longitudinal and transverse cross-section perspectives. Transverse and longitudinal cross-sectional samples are mounted in Bakelite. The samples are prepared on a polishing machine (LaboPol-60, Struers), using lubricants with 9 μm, 3 μm, and finally, 1 μm in size for diamond suspensions and Non-drying fumed 0.25 μm silica suspension for final polishing. For microstructure analysis, a JEOL JSM-7200 Field Emission Scanning Electron Microscope (SEM) equipped with Oxford Instruments EDS and EBSD detectors is utilized [16]. Because an exact longitudinal cut through the bead's centerline cannot be made experimentally, the corresponding simulated longitudinal cross-section was found by laterally shifting cross-sections until the height of the simulated cross-section was the same as the height of the experimental one.

4. Numerical implementation

The present CA model is developed using MATLAB software [73], primarily due to the utilization of vectorized calculations throughout the CA algorithm. CPU parallelization is implemented using MATLAB Parallel Computing Toolbox via the parfor construct (parallel for-loop). The grain growth iterations (loop over all growing cells at each CA timestep) are distributed among available processors. Within each iteration, processors access the CA grid state (cell positions, states, grain indices, octahedron properties) and thermal properties interpolated from the FVM mesh. No explicit inter-processor communication or gather-scatter operations are required because data dependencies are managed through synchronization at loop boundaries: all iterations are computed, then results are synchronized before advancing to the next CA timestep. Load balancing is handled automatically by MATLAB's built-in load balancing scheme, which distributes iterations among available workers to minimize idle time. Specifically, iterations are chunked and assigned to workers dynamically such that workers completing their chunk quickly receive additional iterations, preventing load imbalance. Furthermore, the MTEX toolbox [74] is employed for the analysis and visualization of grain morphology and the assessment of crystallographic texture.

The simulations are conducted in parallel on a workstation equipped with 128 GB of memory and 32 cores of an AMD Ryzen Threadripper 3970X processor operating at 3.70 GHz. An analysis is conducted to examine the dependency of the simulated microstructure on cell size. Fig. 10a shows that a cell size of 5 μm represents the maximum threshold, below which the number of simulated grains becomes independent of the cell size. Fig. 10b shows that the corresponding calculation time exponentially increases when the cell size decreases. This cell size aligns with findings previously reported in the literature [46]. Furthermore, N_V, ΔT_N, and ΔT_σ are set to 10^{14}, 10, and 1, respectively. These values adapted from Refs. [18,67,75] were tuned to reproduce the measured grain sizes while remaining within physically plausible ranges for interface-dominated nucleation in rapid solidification, consistent with the ranges used in literature on AM microstructure modeling.

The thermal-fluid simulation results were stored every 100 μs. This interval was selected to be of the same order as the required time-step so that the solidification front can track the laser scanning speed. Given a laser speed of 20 mm/s in laser melting and a cell size of 5 μm, using a factor of 0.25 yields $0.25 \times (5 \cdot 10^{-6}\ \mathrm{m})/(20 \cdot 10^{-3}\ \mathrm{m\ s^{-1}}) \approx 62.5\ \mu s$. Thus 100 μs ensures sufficiently fine temporal resolution for interpolation from the thermal to the CA domain without coarse loss of data. For the microstructure simulation, the CPU calculation time per cell and the wall-clock calculation time per cell are approximately 320 μs and 900 μs, respectively.

5. Results

5.1. Full track simulation

Fig. 11 (print)/Video 2 (online) shows the simulation of the thermal-fluid dynamics and the solidification microstructure formation during DED-LB along the entire track, using the uniform circular laser beam intensity profile.

5.2. Computational performance analysis

This section analyzes the performance of the optimized thermal-to-CA interpolation method and the CPU-paralleled grain growth algorithm presented in the sections 2.2.2 and 2.2.5.5, respectively.

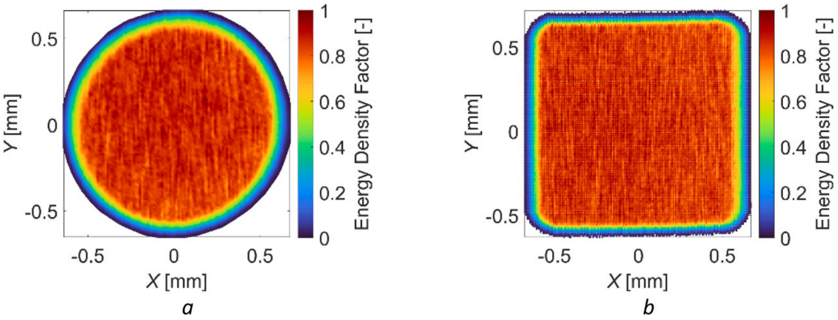

a

b

Fig. 9. Normalized measured energy density profiles of the measured uniform a) circular and b) square laser beam intensity profiles [1,16,71,72].

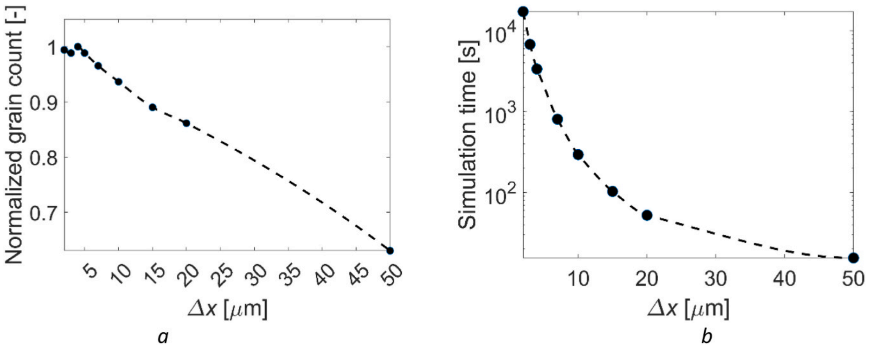

Fig. 10. Dependency of the simulated microstructure, represented by a) the normalized grain count and b) the simulation time, on cell size, with the dashed line serving as a visual aid.

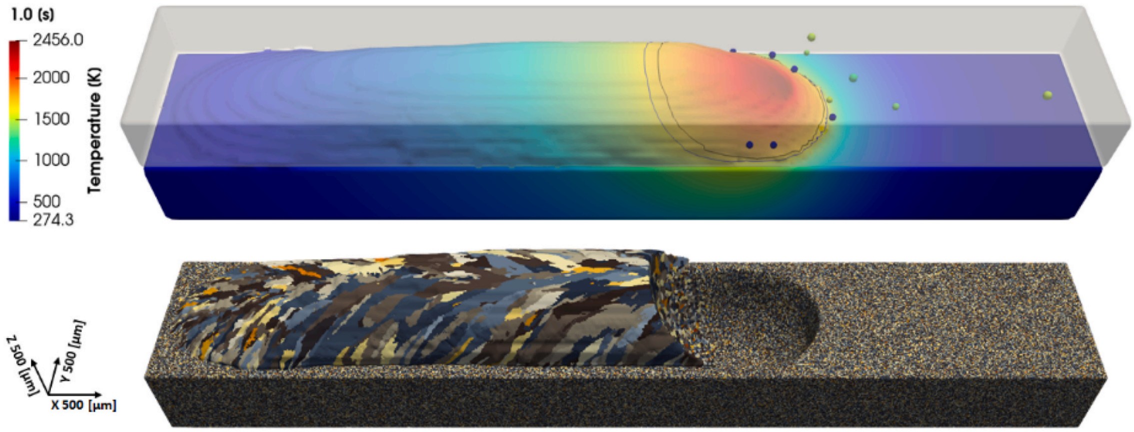

Fig. 11. (print)/Video 2 (online): The thermal-fluid dynamics (top) modeled by Ref. [1] and solidification microstructure formation (bottom) during DED-LB, utilizing the uniform circular laser beam intensity profile.

5.2.1. *Optimized spatial-temporal interpolation*

In this section, the numerical accuracy and computational efficiency of the optimized thermal-to-CA spatial-temporal interpolation method presented in Section 2.2.2, are quantified against non-optimized direct interpolation scheme using the linear scatteredInterpolant MATLAB function. As shown in Fig. 4, in the direct method, the full spatial-temporal interpolation is applied per CA time step. The property is first linearly interpolated between the two enclosing sequential thermal time steps to the current CA time and is then spatially interpolated from the thermal onto the CA grid.

The optimized interpolation scheme preserves exact numerical equivalence to the direct interpolation baseline, verified through cell-wise comparison across the full CA domain and solidification interval. Temperature field shows extremely small maximum cell-wise errors between the two methods across all CA time-steps, with Fig. 12a demonstrating perfect overlap of temperature values at a representative CA time-step (maximum difference: 9.1×10^{-13} K; summed difference: 6.11×10^{-9} K). Fig. 12b shows the equality mask of the metal fraction for all CA cells, defined as a binary field that takes the value 1 where the optimized and direct methods assign the same metal fraction and 0 otherwise; the mask is identically 1, confirming zero deviation in CA domain geometry between both schemes.

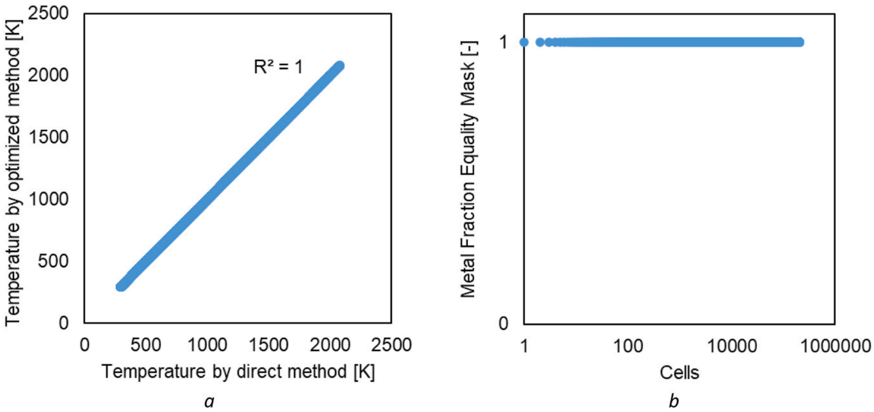

Fig. 12. Comparison of the optimized and direct interpolation schemes at a representative CA time-step for 40 μm size cells discretizing CA domain shown in Fig. 11. (a) Cell temperature values from both methods; (b) Metal fraction equality mask (binary: 1 = identical values, 0 = different).

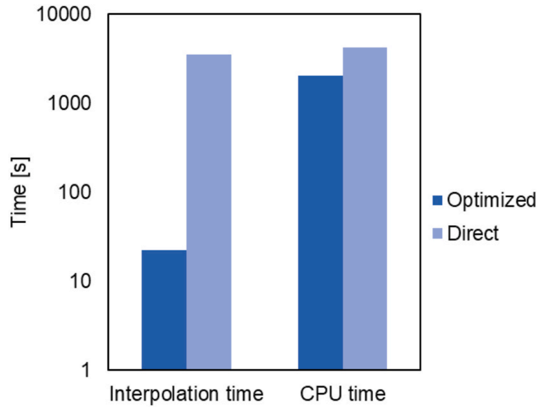

Fig. 13. Interpolation and total CPU times for the optimized versus direct interpolation schemes for the 40 μm discretization of the CA domain shown in Fig. 11.

Despite identical accuracy, the optimized method dramatically reduces computational cost relative to the direct scheme. By precomputing Delaunay tetrahedron assignments and Barycentric coordinates once per cell, spatially interpolating properties to CA field once per thermal time-step, then applying only lightweight linear time interpolation for intra-interval CA updates, the optimized method achieves a computation time reduction by 158x, as shown in Fig. 13. For the 40 μm resolution case (25,0914 cells), the interpolation time dropped from ~3500 s (96.9% of total time) to 22 s (11.3% of total time), eliminating interpolation as a runtime bottleneck. By removing this dominant, the optimized scheme reduces memory stalls and per–time-step overhead in the CA loop, which lowers the total CPU time of the full simulation by a factor of two (Fig. 13), even though the physical model and number of CA time-steps remain unchanged.

5.2.2. *CPU parallelization*

To evaluate the effectiveness of CPU parallelization, a performance study was conducted for the DED-LB domain shown in Fig. 11 discretized by three cell resolutions of 10, 20, and 40 μm and six CPU core counts (1, 2, 4, 8, 16, and 32 cores). Fig. 14a presents simulation time versus CPU core count for 10 μm cell size simulations. Each stacked column separates grain growth algorithm time (light blue) from remaining computation time (dark blue), with total time decreasing from ~8800 s on 1 core to under 5000 s on 4–8 cores—driven solely by grain growth parallelization. This reveals the grain growth algorithm as a significant limit to strong scaling performance, while remaining components comprise efficiently vectorized, MATLAB-optimized calculations. For 20 μm cell size versus 10 μm, calculation times decrease by averaged factors of 6 × (grain growth) and 8 × (remaining parts of the CA model); for 40 μm cell size versus 10 μm, these factors rise to 27 × and 52 × , respectively.

As shown in Fig. 14b, strong scaling analysis reveals non-linear performance characteristics typical of memory-bandwidth-limited applications. Speedup—defined as the ratio of single-core wall-clock time to multi-core wall-clock time—reached an maximum 3.17x (averaged among cell sizes) at 4 cores across all cell sizes for the simulation time of the CPU-parallelized grain growth algorithm, corresponding to parallel efficiency (speedup ÷ number of cores) of 79%, representing the practical limit before overhead dominates execution. Beyond 4 cores, speedup plateaus: at 8 cores, average speedup remained near 3.25x (41% efficiency); at 16 cores, speedup degraded to 1.9 × (12% efficiency); and at 32 cores, speedup collapsed to 1.55 × (5% efficiency). Notably, at 32 cores, wall-clock time increased relative to 4-core performance, demonstrating that additional cores actively worsen performance due to overhead exceeding computational benefit.

For routine simulations, 4-core execution is recommended, providing 3.17x speedup in the grain growth algorithm with modest overhead. This configuration balances acceleration benefit against infrastructure cost and is deployable on standard multi-core workstations. For deadline-critical analyses, 8-core systems offer marginal additional benefit (3.25 × speedup vs. 3.17x) at the cost of significantly higher idle time and efficiency loss (41% vs. 79% for 4 cores). Deployment beyond 8 cores is explicitly not recommended for this algorithm on Non-Uniform Memory Access (NUMA) systems without algorithmic modifications (e.g., domain decomposition, asynchronous parallelization). Therefore, future optimization opportunities include NUMA-aware scheduling, domain decomposition strategies to reduce inter-processor communication, hybrid GPU acceleration of geometric primitives, and memory-efficient data structures to reduce the working set and cache footprint per core.

5.3. *Experimental validation*

5.3.1. *Substrate microstructure*

Fig. 15 presents experimental data on the substrate microstructure. In Fig. 15a, the grains are colored according to their mean crystallographic orientations. Although the substrate exhibits a textured structure (Fig. 15b), this effect is excluded from the simulated substrate to isolate and analyze the specific influence of laser beam shaping on the microstructure. Fig. 15c shows the grain area distribution, with a mean value of ~41 μm^2—equivalent to a square with a size of 6.4 μm—with a standard deviation of 92 μm^2. This equivalent square size value closely matches the limiting cell size of 5 μm calculated in Section 4. The distribution of the ratio of longer to shorter diameters of best-fit ellipses to the grains with the same area (Fig. 15d), as a measure of grain circularity, concentrates near unity, confirming the presence of equiaxed grain morphology, consistent with the substrate microstructure

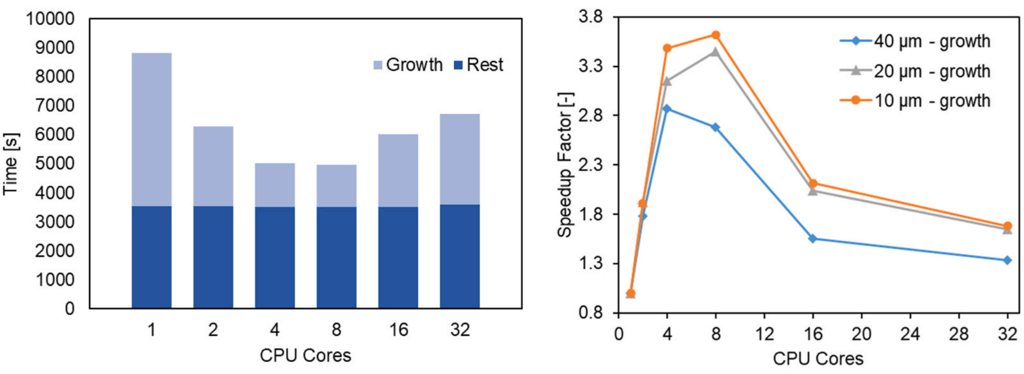

a *b*

Fig. 14. (a) Simulation time vs. CPU cores for 10 μm cells, comparing grain growth (light blue) and remaining time (dark blue); (b) Grain growth algorithm speedup vs. CPU cores for 10 μm (16 M cells), 20 μm (1,9 M cells), and 40 μm (250k cells).

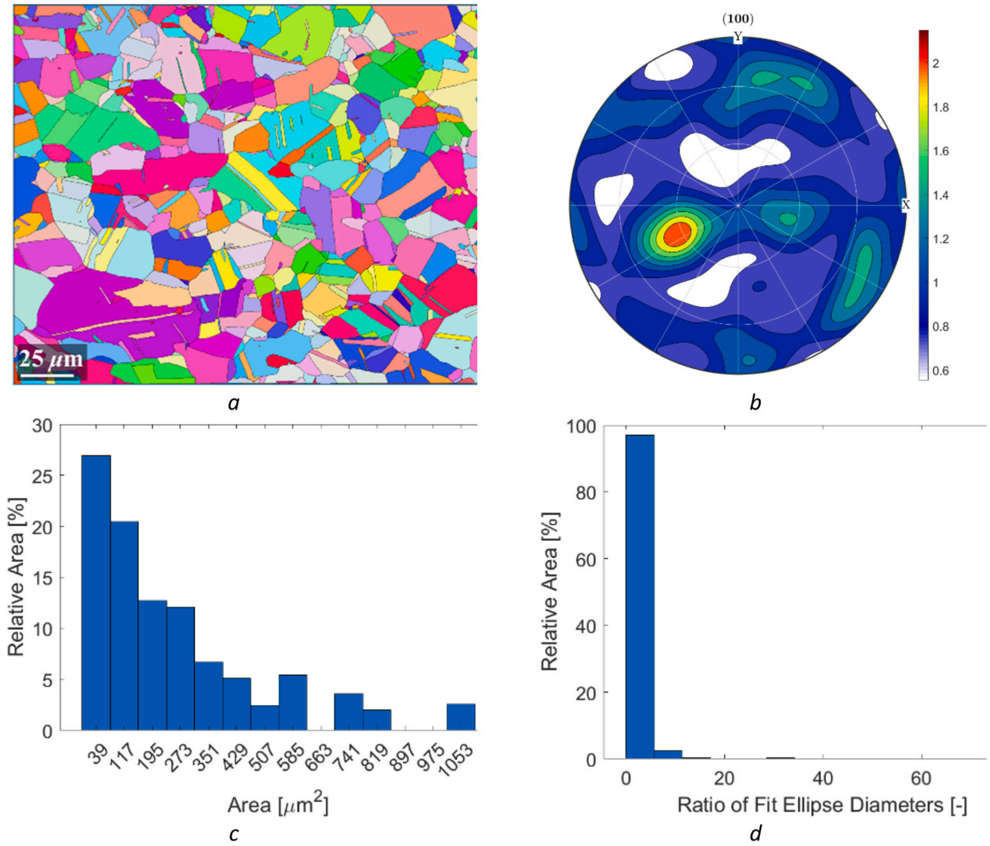

a

b

c

d

Fig. 15. Substrate microstructure analysis; (a) Grains colored by orientation; (b) (100) pole figure; (c) Grain area distribution; and (d) Grain circularity distribution (diameter ratio from equal-area ellipse fitting).

initialization procedure described in Section 2.2.1 and Section 4.

5.3.2. Crystallographic texture

Fig. 16 through Fig. 19 directly compare experimental and simulated cross-sections, pole figures and grain-to-grain misorientation angle distribution quantified via two-sample Kolmogorov–Smirnov statistics for both laser beam shapes and cross-section orientations. Specifically, Fig. 16 shows grain morphology and pole figures of transverse sections for single-track laser melting under uniform circular and square intensity profiles. Figs. 17 and 18 present transverse and longitudinal sections for DED-LB with the uniform circular and square profiles, respectively. Fig. 19 compares misorientation angle distributions across all cases. Finally, Table 2 lists the corresponding texture indices [55] for each case, providing a quantitative measure of crystallographic alignment.

The texture index (Table 2) is a standard measure of the sharpness of the orientation distribution function (ODF) (higher values indicate a stronger texture; values near 1 indicate weak textures). In the present single-track experiments and simulations, the texture indices (≈1.04–1.16) lie in the weak-texture regime, consistent with limited deposited volume and the competing effects of epitaxial growth and heterogeneous nucleation in AM track-scale solidification. Quantitatively, the model reproduces these texture indices with small deviations across all cases: laser melting transverse (3.0% circular; −0.5% square), DED-LB transverse (6.6% circular; 1.0% square), and DED-LB longitudinal (4.6% circular; 10.8% square). These deviations are interpreted as acceptable given that EBSD-based orientation measurements typically have sub-degree angular precision, commonly reported on the order of ~0.5°–1° [76], and ±5% uncertainty in pole figure/ODF reconstruction [77], and ±5% texture measurement bias [78].

For laser melting (transverse), the simulated pole figure (PF) patterns and peak locations and intensities are essentially indistinguishable from experiment (Fig. 16), consistent with the small texture-index deviations reported above. For DED-LB transverse sections by the uniform circular beam (Fig. 17), large experimentally observed columnar grains (highlighted by the dashed boarder and arrow in Fig. 17)—whose <001> axis lies out of plane—are not reproduced, so their anomalous PF peak intensities are absent in the simulation. Importantly, the absence of those extreme PF peaks in the simulation is consistent with the modeling choice to initialize a texture-free substrate in order to isolate beam-shape effects, whereas the experimental substrate exhibits a pronounced pre-existing texture (Fig. 15), which can promote orientation-selective epitaxial growth and amplify PF maxima. Nevertheless, in DED-LB transverse cross-sections for square beam shape and in the longitudinal sections for both beam shapes, no such discrepancies arise; pole-figure patterns, and peak intensities all agree within experimental uncertainty. The minimal deviation between experimental and numerical texture indices, PF patterns, and intensities validates the fidelity of the CA model in capturing texture evolution.

Fig. 19 shows grain misorientation angle probability density functions (PDFs), comparing EBSD (blue) to simulation (red). The misorientation angle distribution is a sensitive descriptor because it depends on the full population of relative grain orientations (not only the dominant PF peaks), and it is affected by both growth selection and the frequency of low-angle vs. high-angle boundaries. The two-sample Kolmogorov–Smirnov (K–S) statistic [79] was applied to compare these distributions where D_{KS} is the maximum vertical distance between the two cumulative distribution functions (CDFs) of two samples; smaller D_{KS} (near 0) means closer distributions, while a large (near 1) indicates difference. The p_{KS} indicates significance, if $p_{KS} < 0.05$, the null hypothesis (that samples are from the same distribution) is rejected. In large EBSD datasets, the K–S test can be extremely sensitive, so very

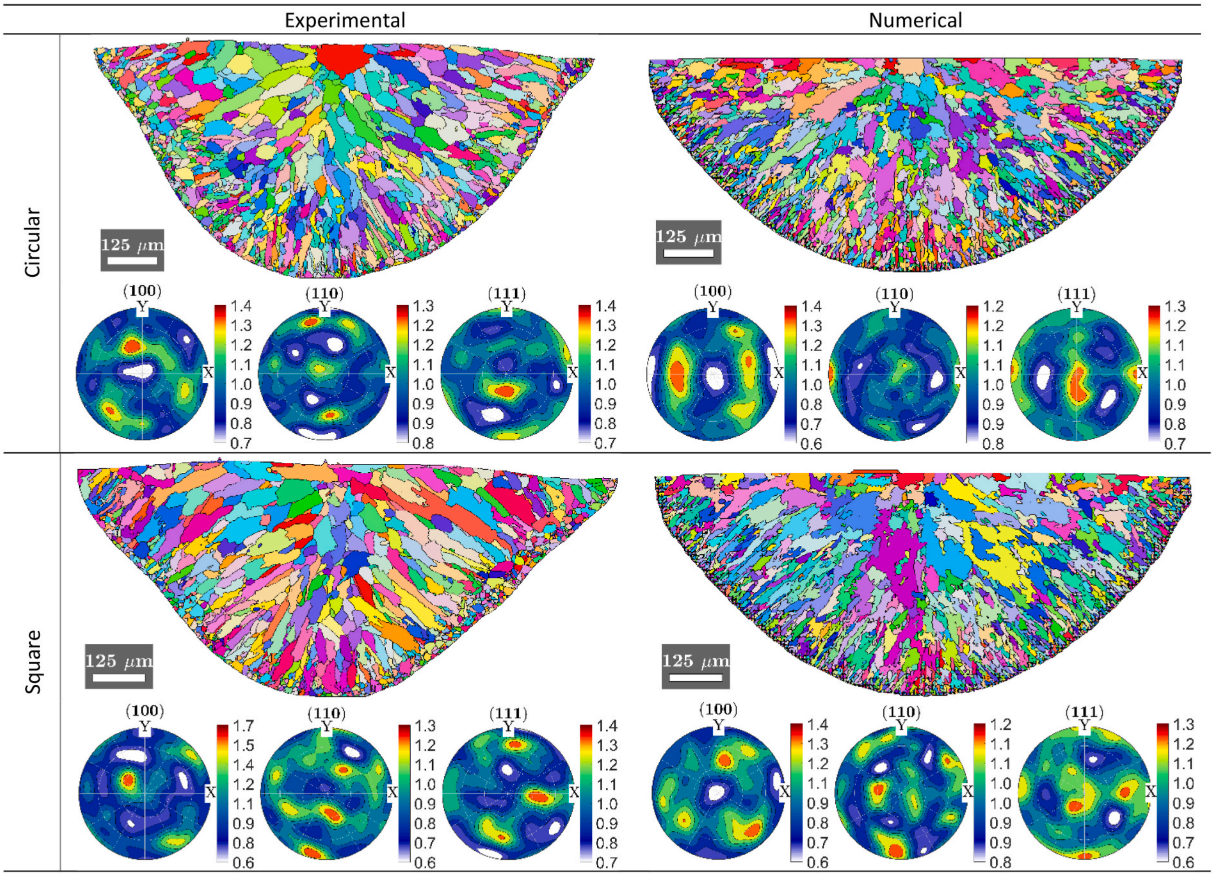

Fig. 16. Grain morphologies and pole figures of transverse sections allowing comparison between experimental (left) and simulated (right) transverse cross-sections of laser melting tracks by the uniform circular and square laser beam intensity profiles.

small differences can still yield p_{KS}-values effectively equal to zero (i.e., "statistically different" does not necessarily imply "practically different"). Therefore, in this section the K–S statistic was used primarily as an effect-size indicator of distribution mismatch (shape and shift differences), rather than as a strict accept/reject hypothesis test.

In the laser melting, transverse, circular case ($D_{KS} = 0.159$), the simulation shows Gaussian-like distribution within 15°–57°, while experiment adds low-angle (3–9°) probability, a 57 peak (PDF ≈ 0.03), and reduced mid-angles; The extra experimental weight at very low misorientations is consistent with EBSD-related sensitivity of "small-angle" statistics to measurement precision and post-processing or segmentation choices (e.g., how sub-grains and low-angle boundaries are treated), which can promote apparent low-angle counts in experimental reconstructions compared with meso-scale CA grains that do not explicitly resolve sub-grain structure. The enhanced experimental high-angle peak near 57° suggests that a specific boundary population is more frequent experimentally than in the model, which is plausible if a small number of strongly selected growth orientations (e.g., near ⟨001⟩ fiber tendencies) compete against the surrounding orientation field and create a characteristic set of high-angle boundaries, shown in Fig. 16 as the large read grain. For the square case ($D_{KS} = 0.383$) with largest mismatch, the simulation is Gaussian-like in 21°–57°, but experiment has strong 3° peak (PDF ≈ 0.05), secondary 57° (PDF ≈ 0.025), and Gaussian-like distribution for mid-angles; this reflects experimental substructure (3–9°) and dominant-orientation high-angles unmodeled in one-orientation-per-grain CA without deformation sub-grains. This pattern (simulated "bulk" misorientation spread versus experimental enrichment of very low and very high misorientations) is consistent with the experiment containing (i) localized regions of small orientation gradients (raising 3–9° bins) and (ii) a limited set of dominant orientations producing frequent high-angle boundaries, neither of which is explicitly represented in a meso-scale CA model that assumes one orientation per grain and does not model deformation-induced sub-grain formation. In addition, this deviation might be introduced by the practical difficulty of extracting a perfectly centered transverse section experimentally, whereas the simulation uses an exact geometric cut; small sampling differences can disproportionately affect distribution tails and low-angle bins. In the DED-LB, transverse and longitudinal, circular and square cases, the patterns similar to the laser melting, transverse, circular case are shown; aligns with manuscript's large out-of-plane columnar grains in experiments (absent from texture-free simulated substrate), reducing the frequency of certain high-angle boundaries and suppresses extreme PF intensities, which naturally propagates into the misorientation PDFs as a weaker high-angle tail/peak. Particularly in for the longitudinal square ($D_{KS} = 0.264$) case, the experimental dominance at 57° (PDF ≈ 0.05) is higher than the other cases in laser melting and DED-LB.

Because the texture index is an orientation distribution function (ODF)-based scalar, it is inherently robust to local outliers yet sensitive to overall alignment, making it a suitable primary validation metric for texture strength. The remaining discrepancies—most apparent as enhanced experimental low-angle (3–9°) content and amplified high-angle peaks near 57–60°—are consistent with known limitations of (i) EBSD small-misorientation reliability/segmentation sensitivity and (ii) meso-scale CA texture modeling choices that omit sub-grain structure and, in this study, intentionally remove substrate texture to isolate beam-shape effects; both factors can shift boundary statistics while preserving the dominant pole figure peaks and overall ODF sharpness. Finally, the consistently small K–S statistics (typically 0.118–0.159 except for the laser-melting square and DED-LB longitudinal square

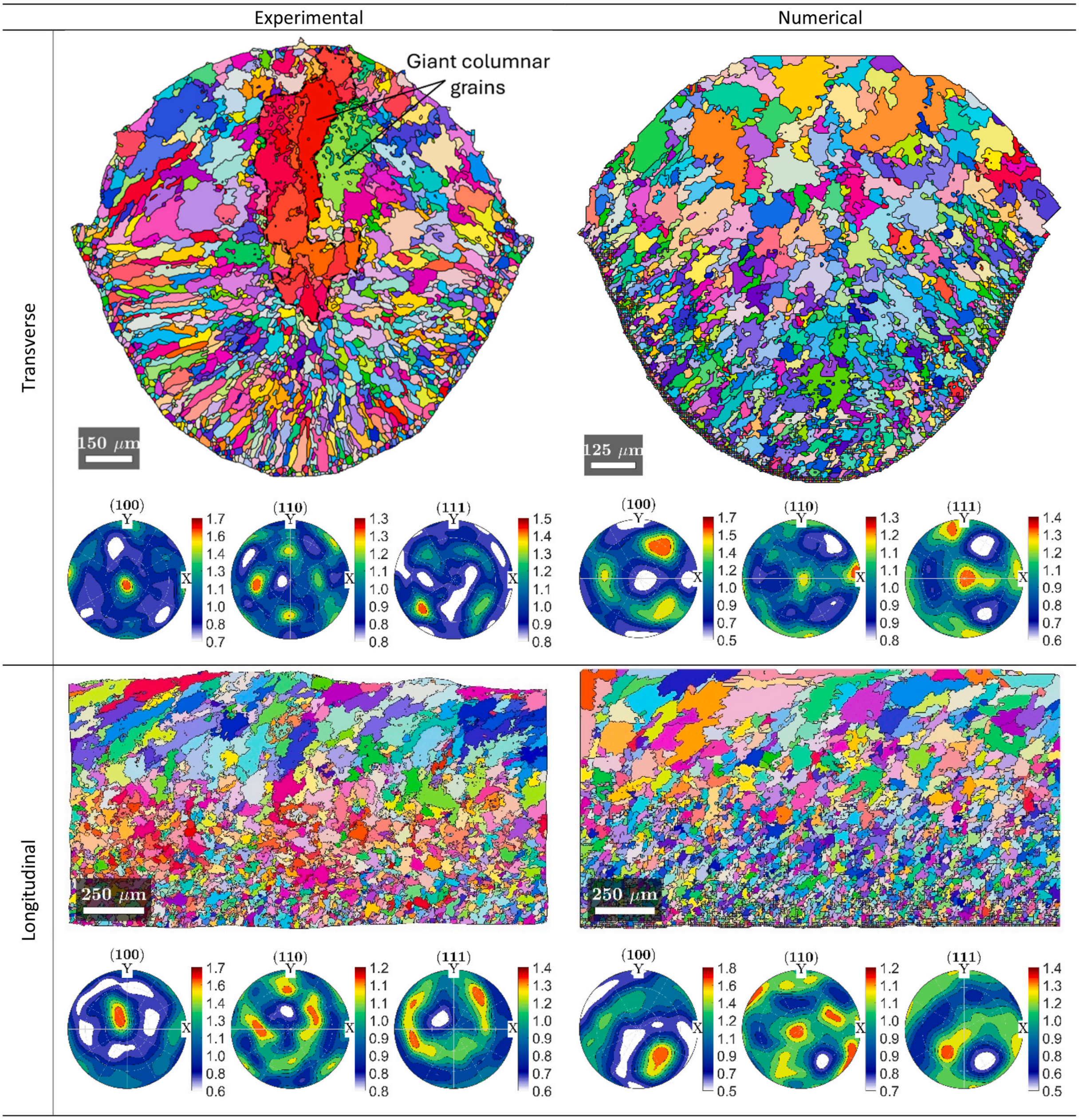

Fig. 17. Grain morphologies and pole figures allowing comparison between experimental (left) and simulated (right) transverse and longitudinal cross-sections of DED-LB tracks by the uniform circular laser beam intensity profile.

cases) indicate that the CA model captures the main shape of the misorientation distributions, while $p_{KS} \approx 0$ are expected for large EBSD datasets and should be interpreted as high sensitivity rather than practical failure of the model.

5.3.3. Grain morphology

Fig. 20 compares the simulated (red bars) and experimentally measured (blue bars) distributions of grain area and the ratio of longer to shorter diameters of best-fit ellipses with the same area at each cross-section introduced in the previous section. Quantitative agreement is evidenced by close central tendency and spread—e.g., in the laser melting, transverse cross-section, circular beam case: experimental area means 152 ± 405 μm^2 equivalent to a circle diameter of 13.9 μm versus 125 ± 379 μm^2 simulation area equivalent to 12.6 μm circle diameter (9.2% error), with diameter ratios 2.04 ± 0.932 experimentally versus 1.95 ± 0.905 numerically (4.4% error). For square beam: 67.6 ± 295 μm^2 equivalent to 9.3 μm circle diameter experimentally versus 104 ± 517 μm^2 equivalent to 11.5 μm circle diameter (23.6% error) numerically, with 1.92 ± 0.904 experimental ratio versus 1.82 ± 0.898 numerical ratio (5.2% error)—and similar for all other cases. For DED-LB of the circular beam, 24.1% error in equivalent diameter and 19.9% error in diameter ratio are found for the transverse cross-section and 8.9% and 11.8%, respectively, for the longitudinal one. In DED-LB with square beam, these values are 20.9% error in mean diameter, 15.4% error in diameter ratio for transverse, and 8.3% error in mean diameter, 14.8% error in diameter ratio for longitudinal cross-sections; all $p_{KS} \approx 0$ due to large sample sensitivity [79].

As can be concluded from the distribution graphs in Fig. 20, overall, the simulation reproduces the experimental distributions with high fidelity, despite mean shifts. Notable discrepancies in the distribution arise only for the transverse section in DED-LB build with a circular beam profile (Fig. 17). This region exhibits a few exceptionally giant and many small grains (highlighted by the dashed boarder and arrow in Fig. 17), all with preferred <100> orientation parallel to the build

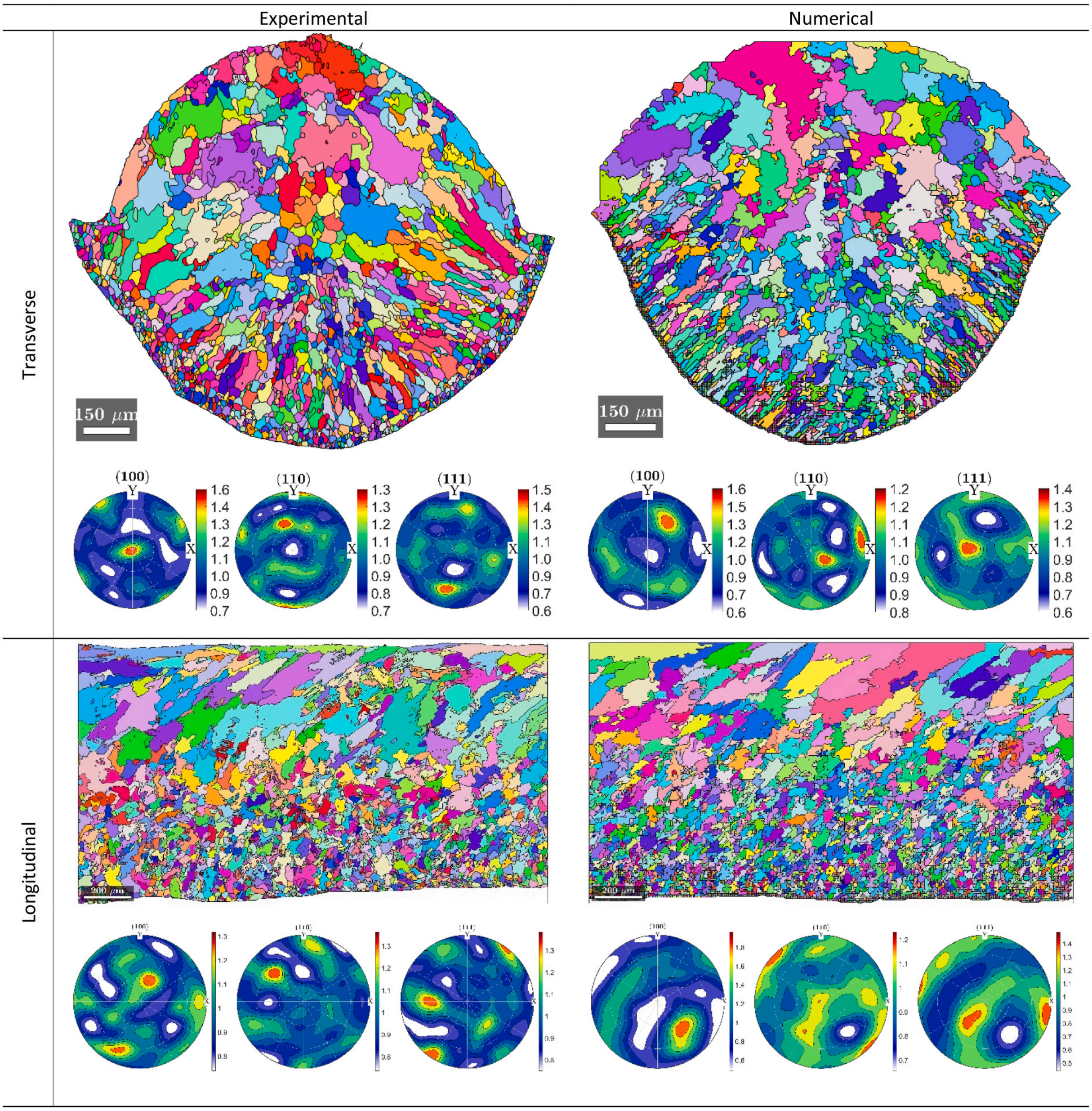

Fig. 18. Grain morphologies and pole figures allowing comparison between experimental (left) and simulated (right) transverse and longitudinal cross-sections of DED-LB tracks by the uniform square laser beam intensity profile.

direction, which are absent in the simulation. This limitation primarily stems from the strong ⟨100⟩ fiber texture in the experimental substrate, as revealed by pole figure analysis in Fig. 15b. Such texture selectively promotes epitaxial growth of ⟨100⟩-oriented grains from favorably aligned substrate nuclei, yielding these giant columnar structures. In contrast, the simulations employed a texture-free substrate initialization (Section 2.2.1), precluding such orientation-specific selection and resulting in a higher fraction of equiaxed grains. In addition, the melt pool tail experiences local variations in convective heat transfer that can selectively stabilize growth fronts for favorably oriented nuclei [71]. The weak one-way coupling scheme further contributes by smoothing transient melt pool dynamics, including Marangoni convection in the tail region where these grains form. This prevents thermodynamical differentiation between favorably and unfavorably oriented nuclei competing under similar undercooling conditions, preventing the sustained growth advantage necessary for exceptional grain structures.

Future work incorporating sensitivity studies on orientation-weighted grain capture criteria or full transient thermal coupling would extend predictive capability to encompass rare, crystallographically selected microstructural features while maintaining computational efficiency. Apart from this, the minimal deviation between experimental and numerical grain area and best-fit ellipse aspect ratio validates the fidelity of the CA model in capturing grain morphology evolution.

6. Discussion

The present investigation reveals that laser beam intensity profile influences solidification microstructure. At the macroscopic level, the beam intensity profile directly determines the spatial distribution of energy input (absorbed laser energy), which cascades through multiple length scales to affect grain nucleation, competitive growth, and final microstructure characteristics. Previously, we [1] demonstrated that the beam geometry significantly affects melt pool characteristics. The square-shaped laser beam, with lower laser energy attenuation and a larger irradiation surface, creates a wider, longer and larger melt pool with lower peak temperature compared to a circular beam, resulting in

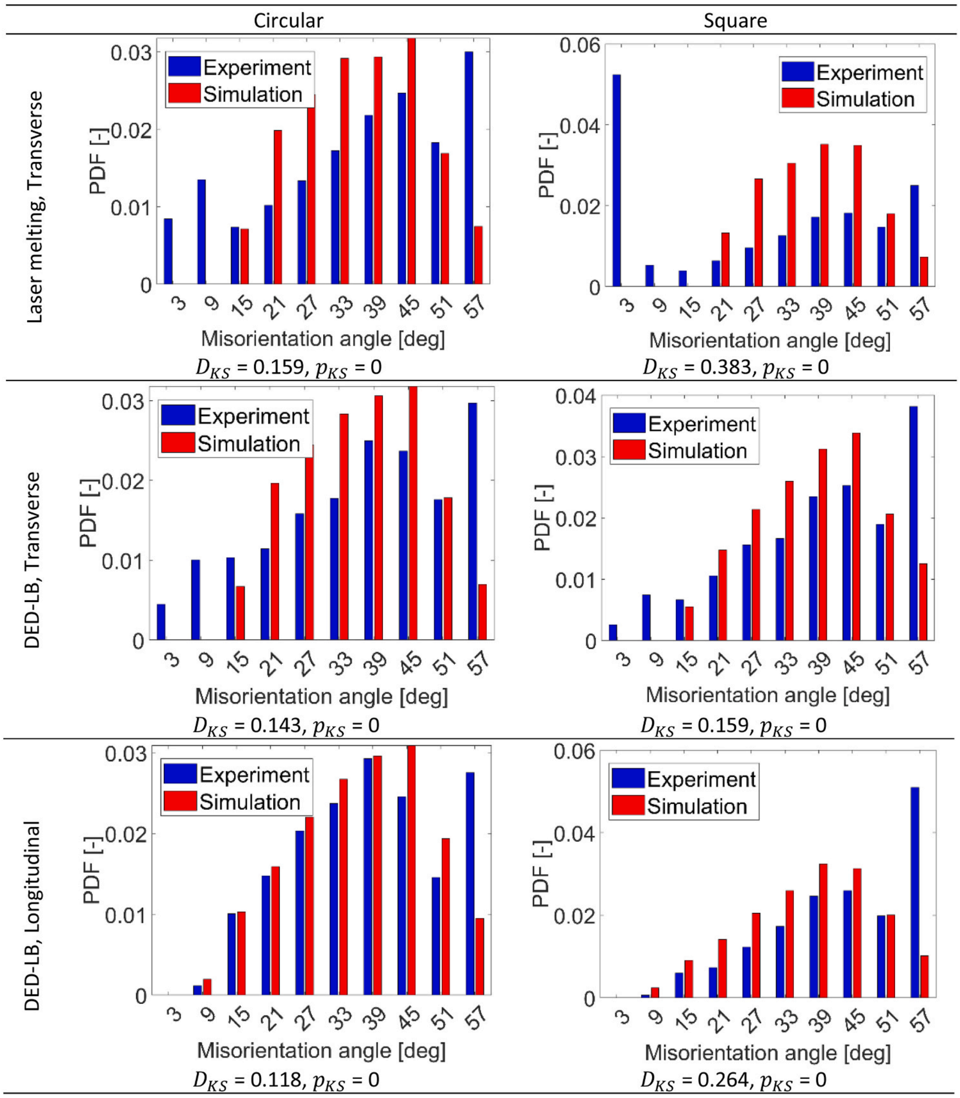

Fig. 19. Experimental (blue) vs. simulated (red) grain misorientation angle distributions and their K–S statistical results for the transverse and longitudinal cross-sections of laser melting and DED-LB tracks, using uniform circular and square beam profiles.

Table 2
Comparison of the texture index for experimental and simulated transverse and longitudinal cross-sections of laser melting and DED-LB tracks by the uniform circular and square laser beam intensity profiles.

Process	Laser beam shape	Cross-section	Experimental	Numerical	Deviation [%]
Laser Melting	Circular	Transverse	1.039	1.071	3.0
	Square	Transverse	1.092	1.086	−0.5
DED-LB	Circular	Transverse	1.068	1.139	6.6
		Longitudinal	1.094	1.145	4.6
	Square	Transverse	1.067	1.078	1.0
		Longitudinal	1.049	1.163	10.8

more uniform temperature distributions. However, the circular profile generates a higher peak temperature and faster fluid velocity, resulting in a deeper melt pool. The higher Peclet number for the circular beam underscores the heightened role of fluid flow in energy transfer, leading to a deeper melt pool compared to the square beam. Moreover, the higher Marangoni number for the circular beam highlights the dominance of surface shear stress over viscous forces, resulting in faster fluid flow within the melt pool. The smaller melt pool with higher peak temperature means having steeper radial temperature gradients in that melt pool generated by the circular beam shape [1]. These differences in melt pool geometry directly influence the solidification parameters G (temperature gradient) and R (solidification rate), which govern microstructure evolution according to classical solidification theory [80]. The $G{\cdot}R$ product, representing cooling rate, controls grain size, while the G/R ratio determines grain morphology, with higher values promoting columnar growth [18].

6.1. Crystallographic texture sensitivity to the laser intensity profile

The experimentally measured pole figures in Fig. 16 demonstrate that peak intensities related to the transverse cross-sections are marginally lower for the square beam compared to the circular beam in

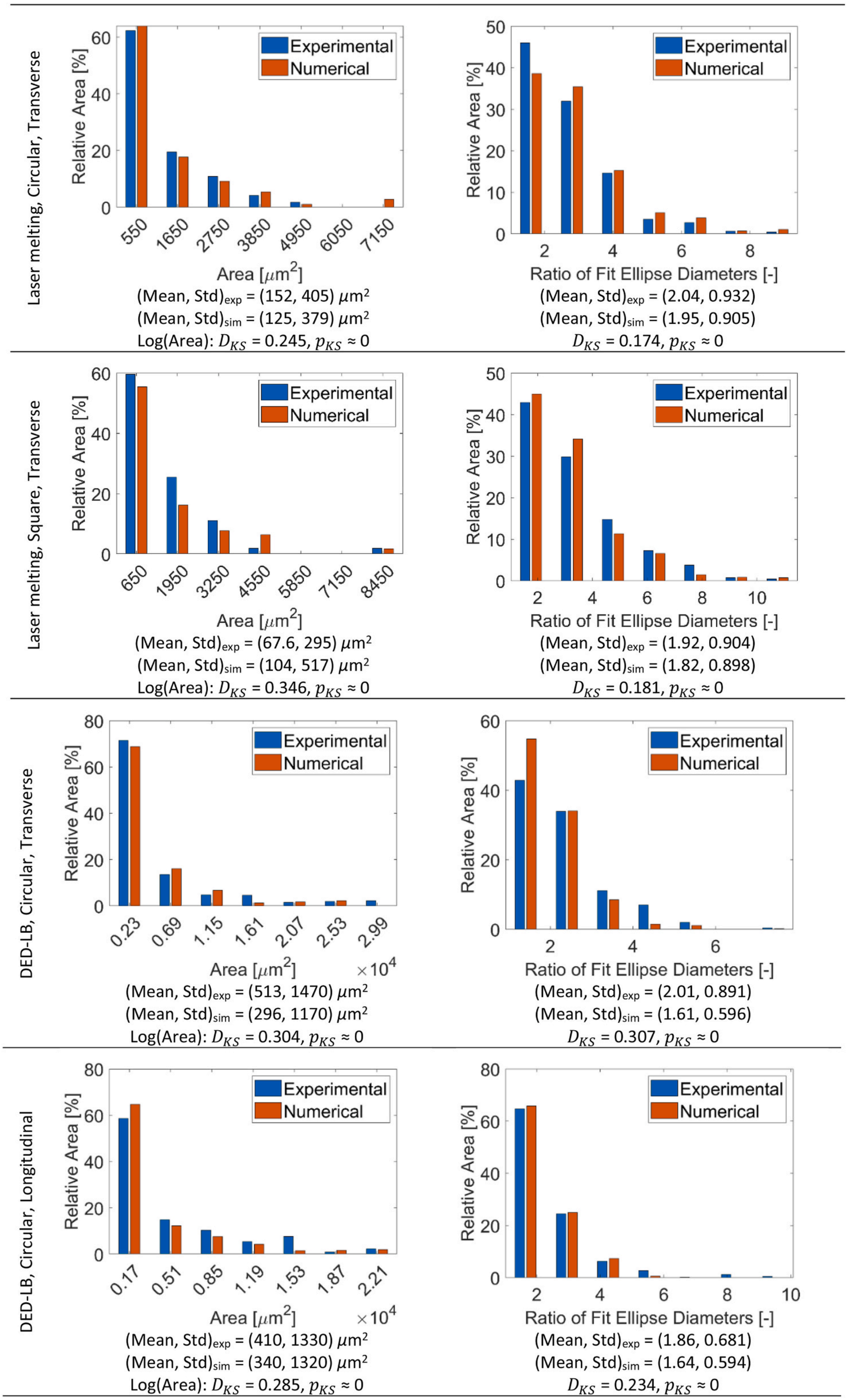

Fig. 20. Comparison of the experimental (blue bars) and simulated (red bars) distributions of grain area and grain aspect ratio—defined as the ratio of the longer to shorter diameters of the best-fit ellipse with the same grain area—across the transverse and longitudinal cross-sections for both uniform circular and square laser beam intensity profiles in laser melting and DED-LB. The vertical axis in each plot represents the percentage of the total cross-sectional area occupied by grains within each size or aspect ratio bin.

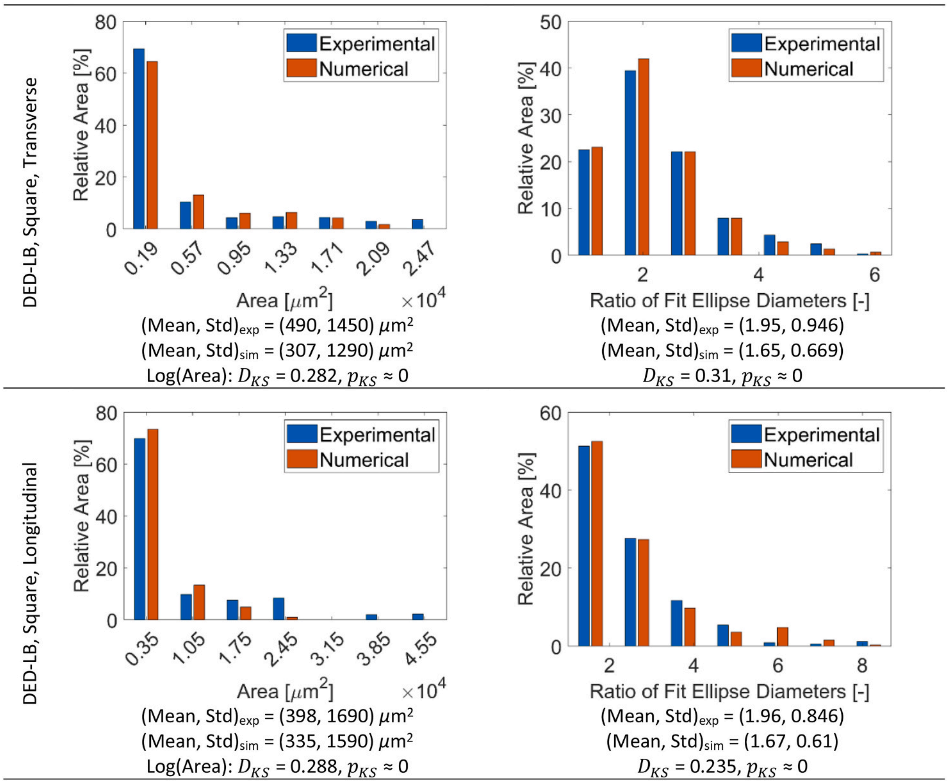

$(\text{Mean, Std})_{exp}$ = (490, 1450) μm^2
$(\text{Mean, Std})_{sim}$ = (307, 1290) μm^2
Log(Area): $D_{KS} = 0.282$, $p_{KS} \approx 0$

$(\text{Mean, Std})_{exp}$ = (1.95, 0.946)
$(\text{Mean, Std})_{sim}$ = (1.65, 0.669)
$D_{KS} = 0.31$, $p_{KS} \approx 0$

$(\text{Mean, Std})_{exp}$ = (398, 1690) μm^2
$(\text{Mean, Std})_{sim}$ = (335, 1590) μm^2
Log(Area): $D_{KS} = 0.288$, $p_{KS} \approx 0$

$(\text{Mean, Std})_{exp}$ = (1.96, 0.846)
$(\text{Mean, Std})_{sim}$ = (1.67, 0.61)
$D_{KS} = 0.235$, $p_{KS} \approx 0$

Fig. 20. (*continued*).

Table 3
The difference percentage of the texture index for experimental and simulated transverse and longitudinal cross-sections of laser melting and DED-LB tracks by the uniform circular and square laser beam intensity profiles.

Process	Cross-section	Dataset	Texture Index Difference Percentage [%]
Laser Melting	Transverse	Experimental	+5.1
		Numerical	+1.4
DED-LB	Transverse	Experimental	−0.1
		Numerical	−5.3
	Longitudinal	Experimental	−4.1
		Numerical	+1.5

laser melting. However, the corresponding texture indices listed in Table 2 are slightly higher for the square profile. A comparable trend emerged in the DED-LB investigations when comparing the results shown in Figs. 17 and 18 for these two beam shapes. Pole figures for both the transverse and longitudinal cross-sections reveal slightly reduced peak intensities for the square beam relative to the circular beam, and the associated texture indices displayed only negligible deviations. Quantitatively, the percentage differences between square- and circular-beam induced texture indices are summarized in Table 3. Overall, within the present case studies, the texture variations attributable to beam profile are minor, indicating that despite significant differences in melt pool geometry and thermal conditions, previously reported in Ref. [1], crystallographic selection mechanisms during solidification are relatively insensitive to variations in the beam profile.

The texture indices measured or simulated (ranging from 1.039 to 1.163) fall within the typical range for single-track AM experiments. Comparison with literature values reveals consistent trends with other studies. For instance, Zinovieva et al. [13] reported texture indices increasing from 1.08 to 1.79 with build height in selective laser melting of 316L steel. The relatively weak texture in the present single-track experiments reflects the limited volume of material experiencing directional solidification and the influence of the randomly oriented nucleation and substrate grains.

6.2. Beam shaping effects on grain morphology

In contrast to texture, grain morphology exhibits stronger sensitivity to variations in the beam intensity profiles. Fig. 21 compares the measured and simulated grain area and aspect ratio histograms for the circular and square beam shapes. The circular beam produces finer and more equiaxed grain structures in transverse sections for laser melting both experimentally and numerically. The same trend is observed for DED-LB in the numerical results for both transverse and longitudinal cross-sections and in the experimental results for the longitudinal cross-sections. But the corresponding experimental results on the transverse cross-sections do not follow this trend. Initially, the substrate grains were visually removed from the experimental cross-sections by estimating the melt-pool boundary from changes in grain size and morphology. This visual method may have allowed a small number of fine and equiaxed substrate grains to enter the dataset, modestly elevating the fine-grain count. As shown in Fig. 18, specifically on the transverse cross-sections, these grains around the boundary of the melt pool in the substrate are a bit more numerous for the square laser beam. Because the numerical model defines the fusion boundary automatically (not visually), its transverse grain statistics are considered the more robust reference for evaluating the beam-shape effect in this instance. With this consideration, the circular beam consistently produces finer and more equiaxed grain structures. As described in Section 6, this morphological difference can be attributed to the finding that the steeper radial temperature gradients in circular beam profiles create higher cooling rates ($G \cdot R$) at the solidification front, promoting grain refinement through increased nucleation rates and reduced growth times [11].

On the other hand, Fig. 20 shows that uniform square beam profiles experimentally produce smaller mean grain areas in laser melting and slightly smaller mean areas in DED-LB. These results are consistent with

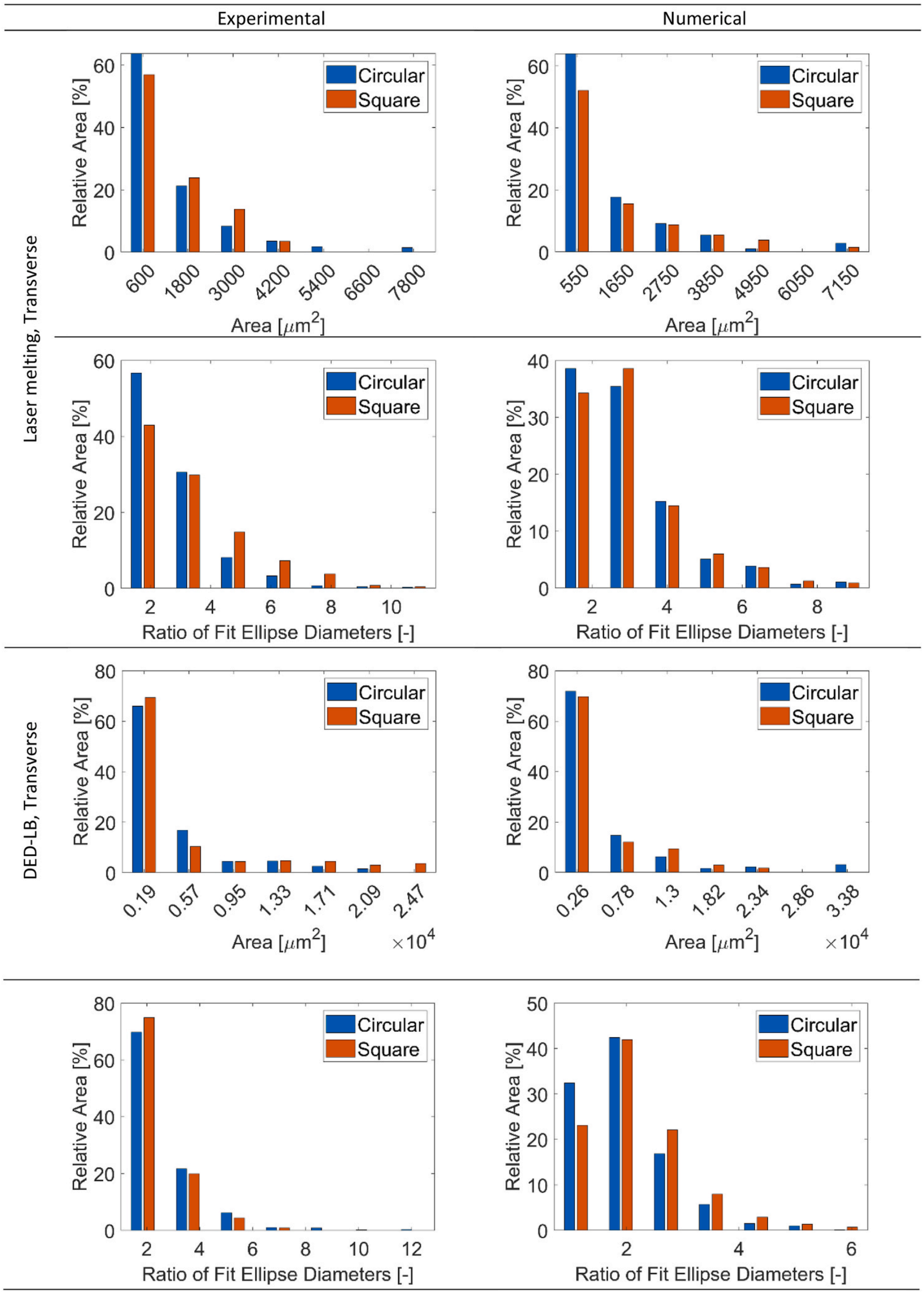

Fig. 21. Comparison of the effect of uniform circular (blue bars) and square (red bars) laser beam intensity profiles on the experimental and simulated distributions of grain area and grain aspect ratio—defined as the ratio of the longer to shorter diameters of the best fit ellipse with the same grain area—across the transverse and longitudinal cross-sections for in laser melting and DED-LB. The vertical axis in each plot represents the percentage of the total cross-sectional area occupied by grains within each size or aspect ratio bin.

similar findings in literature [16]. However, the significance of beam shaping effects on grain size clearly decreases from laser melting to DED-LB, and this trend does not hold in DED-LB by simulation. As mentioned at the start of this section, uncertainty arising from the inclusion of substrate grains in the experimental analysis can be significant, whereas the simulations are not affected by this sampling issue. Furthermore, equiaxed tendency (lower aspect ratio) is process- and section-dependent: the square beam yields more equiaxed grains in laser melting but higher aspect ratios (more columnar) in DED-LB, both experimentally and numerically, compared to the circular beam. Importantly, mean values of grain area and aspect ratio are poor representatives of the full morphology distributions, as rare large outliers (e.g., giant columnar grains) disproportionately skew the arithmetic means and standard deviations.

The thermal-fluid model helps calculate the temperature gradient $\left(\overrightarrow{G}\right)$, which is determined by Ref. [18],

$$\overrightarrow{G} = \overrightarrow{\nabla T} = \left(\frac{\partial T}{\partial x}, \frac{\partial T}{\partial y}, \frac{\partial T}{\partial z}\right). \tag{39}$$

On the other hand, in the quasi-steady-state in the laser process, where the size and shape of the melt pool are stable and do not change

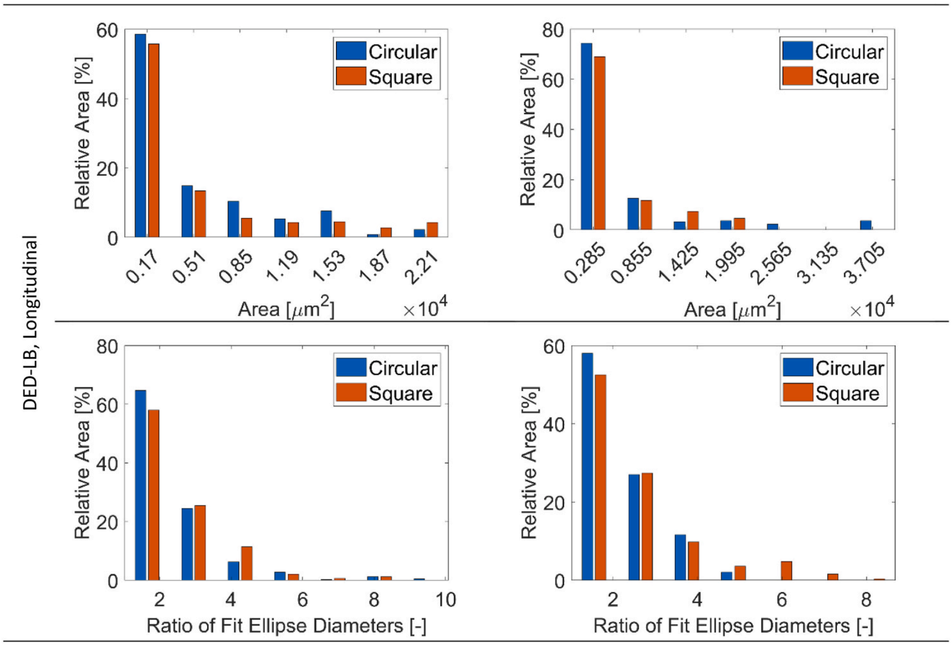

Fig. 21. (*continued*).

while the laser beam scans the material, a geometric relationship is applied between the solidification front velocity ($\vec{R}$) and the laser beam scanning velocity ($\vec{v_l}$), expressed as $\left\|\vec{R}\right\| = \|\vec{v_l}\|\cdot\cos\theta$, where θ is the angle between the scanning direction and the heat flow direction [18]. Considering the "planar" G as well as R, G/R determines the grain morphology with a higher value resulting in a more columnar grain, while $G{\cdot}R$ representing the cooling rate controls the grain size with a higher value resulting in smaller grain with narrow dendrite arm spacing [81,82].

Fig. 22 compares the numerical transverse cross-sections color-coded by grain area and $G{\cdot}R$ contour as well as by grain aspect ratio and G/R contour for the uniform circular and square beam profiles in laser melting and DED-LB. The $G{\cdot}R$ and G/R maps are two-dimensional projections of these values for cells on the transverse cross-sections at the moment of solidification within the three-dimensional mushy zone. It is consistently observed that higher values of the product $G{\cdot}R$ correspond to smaller grain sizes across all cross-sections. In the top central region of the cross-sections—which locates near the melt pool tail—the cooling rate is lowest (heat is transferred to the yet-warm previously scanned surface or deposited material), therefore, the largest grains are formed. In contrast, at the bottom boundaries—where the cooling rate is highest due to the maximum heat conduction—smaller grains are found. Additionally, the presence of very fine grains in the substrate contributes to maintaining smaller grain sizes in the melt track through epitaxial growth. Regions with higher G/R values promote the formation of columnar grains, which grow radially inward from the bottom cross-section (melt pool) boundary toward the center. Conversely, at the top center of the cross-section—where heat conduction is minimum, heat flow is symmetric, and the temperature gradient is at a minimum—lower G/R values result in more equiaxed grain structures.

The influence of beam shape is also evident from Fig. 22. That is, the use of a square beam shape results in 1000 K/s and 100 K/s lower cooling rates ($G{\cdot}R$) in both the laser melting and the DED-LB process, respectively, which leads to the formation of larger grains at the center of the cross-section compared to the circular beam shape. Furthermore, the square beam produces higher G/R ratios in laser melting, which in turn generates grains with higher aspect ratios throughout the cross-section. However, in the DED-LB process, these two beam shapes do not pose significant differences. The influence of beam shaping on both $G{\cdot}R$ and G/R decreases in DED-LB, predominantly owing to the attenuating effects of powder feeding—which reduces effective absorptivity and dilutes incident energy density—and continuous material deposition, which acts as a dynamic heat sink and homogenizes local thermal gradients.

These findings confirm that the CA model reliably reflects the thermal fields predicted by the thermal-fluid simulations, demonstrating the accuracy and consistency of the CA approach with respect to the underlying physical processes.

7. Conclusion

In this study, an optimized high-fidelity computational framework was developed and validated that couples thermal-fluid dynamics to a microstructure model for investigating laser beam shaping effects on solidification microstructure in laser melting and directed energy deposition (DED-LB). The integrated modeling approach enabled computationally tractable simulations of full-track solidification while maintaining the spatial resolution necessary for accurate microstructure prediction. The key novelties of this approach include CPU-parallelized grain growth algorithms, spatiotemporal optimization, a fast thermal-to-CA interpolation scheme, and adaptive CA time-step control.

The optimized thermal-to-CA interpolation, based on pre-computed Delaunay tetrahedra and barycentric weights with minimum spatial interpolation and linear temporal interpolation, was numerically identical to the direct thermal-to-CA interpolation, while reducing interpolation time by about 158 × and total CA simulation time by roughly a factor of two. CPU-parallelized grain growth exhibits strong scaling up to 4 cores, achieving an average 3.17 × speed-up (≈79% efficiency), with smaller incremental gains beyond 8 cores due to memory-bandwidth and overhead limitations.

Through simulation and experimental validation of single-track laser melting and DED-LB processes using uniform circular and square laser beam intensity profiles, the model demonstrated excellent predictive accuracy. Simulated texture indices closely matched experimental results, with deviations ranging from −0.5% to +10.8%, confirming the fidelity of the crystallographic orientation modeling. Across all laser melting simulations, the simulated pole figure patterns and peak intensities were indistinguishable from experiments, with texture index deviations of just 3.0% (circular) and −0.5% (square). For the more

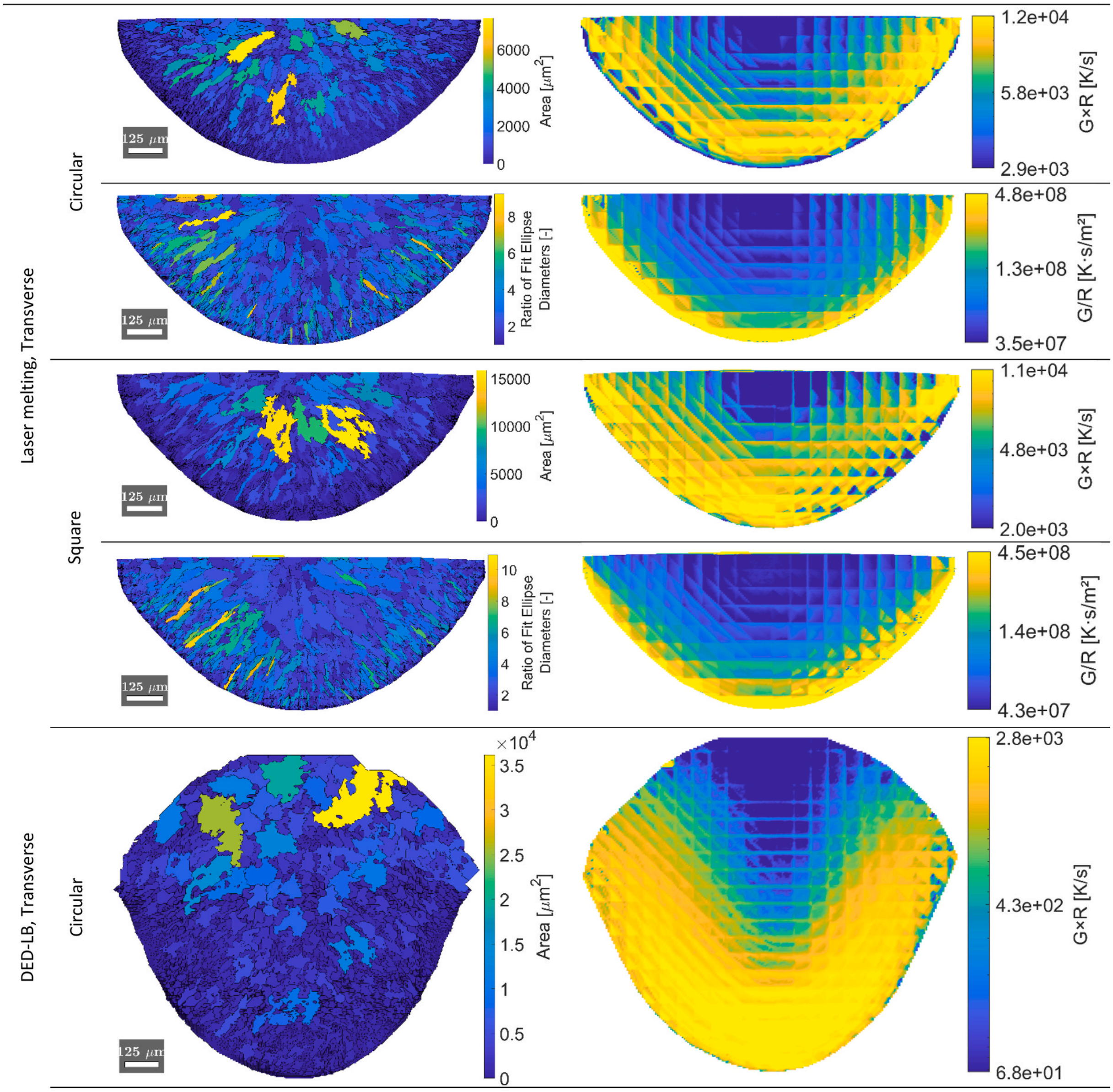

Fig. 22. Simulated transverse cross-sections of laser melting and DED-LB tracks, with grains color-coded by area and aspect ratio (longer/shorter diameters of best-fit ellipse). 2D-projected $G{\cdot}R$ and G/R maps from the 3D mushy zone at the solidification moment of cross-section cells.

complex DED-LB process, transverse sections yielded deviations of 6.6% (circular) and 1.0% (square), while longitudinal sections showed deviations of 4.6% (circular) and 10.8% (square). Texture index deviations ($\leq$10.8%) fall within EBSD experimental uncertainty, confirming model fidelity.

The investigation revealed that texture development shows limited sensitivity to beam profile variations, with texture index differences between circular and square beams ranging from -5.3% to $+5.1\%$. These results indicate that, despite varying beam profiles and melt pool geometries, texture development is primarily governed by epitaxial growth and similar G/R ratios at the solidification front for both beam profiles.

However, grain morphology exhibited a stronger dependence on beam shape. Based on the grain area and aspect ratio distributions, circular beam profiles consistently produced finer and more equiaxed grain structures in both laser melting and DED-LB processes, as observed in both transverse and longitudinal cross-sections. This morphological refinement is attributed to the mechanism that steeper radial temperature gradients in circular beams produce higher cooling rates ($G{\cdot}R$), enhancing nucleation rates and shortening grain growth durations. Comparing the simulated and experimentally measured distributions of grain area and best-fit ellipse aspect ratios, the simulation reproduced experimental distributions with near-perfect fidelity. On the other hand, uniform square beam profiles experimentally produce smaller mean grain areas than circular beams in laser melting and slightly smaller areas in DED-LB, a trend that is generally captured by the simulations, albeit with weaker and cross-section-dependent differences in DED-LB. Mean grain area and aspect ratio are, however, poor representatives of the full morphology distributions, since rare large columnar grains strongly skew these metrics.

Further analysis revealed that regions with higher $G{\cdot}R$ values consistently exhibited smaller grain sizes, while lower $G{\cdot}R$ values—typically near the top center of the melt track—led to larger, more equiaxed grains. A higher G/R ratio was associated with columnar grain growth, especially from the bottom fusion boundary upward, whereas large equiaxed grains formed near the surface where temperature gra-

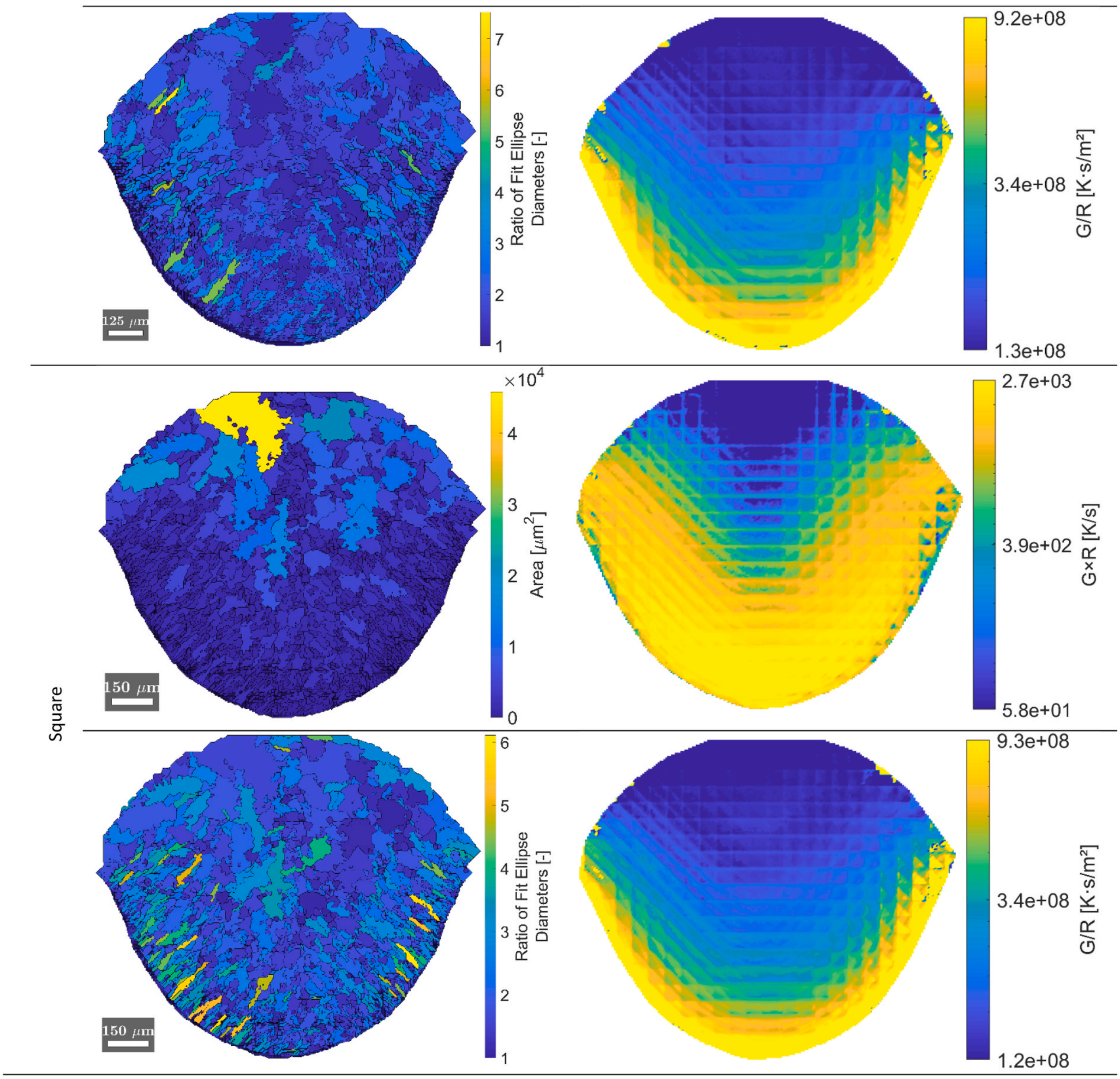

Fig. 22. (*continued*).

dients and cooling rates were minimal.

The influence of beam shape was especially pronounced. In both processes, the square beam produced a lower minimum value of $\cdot R$, resulting in larger central grains in the cross-section compared to the circular beam. While square beams generated higher average G/R ratios—producing grains with greater aspect ratios in laser melting—DED-LB exhibited a more favorable aspect ratio distribution when using circular beams.

The results presented herein are specific to single-track DED-LB of 316L austenitic stainless steel under the chosen process parameters. Future investigations include beam shaping effects across diverse alloy systems spanning the thermal properties spectrum, varied laser power and scanning velocity, and pre-heated or multi-layer geometries. Overall, the model provides a reliable and efficient way to explore how laser parameters affect microstructure formation. It can support the design of additive manufacturing processes to control grain structure, reduce anisotropy, and improve final part performance. With its accuracy and efficiency, this tool can play a valuable role in developing digital twins and guiding process optimization in real AM applications.

CRediT authorship contribution statement

Conceptualization, M.S.; Methodology, M.S., A.E., M.L., G.R.B.E.R.; Software, M.S.; Validation, M.S.; Formal analysis, M.S.; Investigation, M.S.; Resources, M.S., M.L., G.R.B.E.R.; Data curation, M.S.; Writing—original draft preparation, M.S.; Writing—review and editing, M.S., A.E., M.L., G.R.B.E.R.; Visualization, M.S.; Supervision, M.L., G.R.B.E.R.; Project administration, M.S., M.L., G.R.B.E.R.; Funding acquisition, G.R.B.E.R.

Declaration of generative AI and AI-assisted technologies in the manuscript preparation process

During the preparation of this work the authors used ChatGPT and Claude in order to revise text grammar and improve writing clarity. After using these tools, the authors reviewed and edited the content as needed and take full responsibility for the content of the published article.

Declaration of competing interest

The authors declare that they have no known competing financial interests or personal relationships that could have appeared to influence the work reported in this paper.

Acknowledgment

The authors thank Nick Helthuis for assistance with EBSD measurements.

The study was performed as a component of the Aim2XL program, which is part of the collaborative Partnership Program between the Netherlands Organization for Scientific Research (www.nwo.nl) and the Materials Innovation Institute M2i (www.m2i.nl), and was designated by project number P16-46/S17024i. The authors would like to thank the industrial partners, including the Rotterdam Fieldlab Additive Manufacturing BV (RAMLAB) (www.ramlab.com).

Appendix A. Supplementary data

Supplementary data to this article can be found online at https://doi.org/10.1016/j.jmrt.2026.02.190.

Data availability

This study's raw or processed data, necessary to reproduce the reported findings, cannot be shared at the moment due to their large size. However, representative samples of the research data are provided in this paper. Any additional datasets generated during this study are available upon reasonable request from the corresponding author.

References

[1] Sattari M, Ebrahimi A, Luckabauer M, Römer GRBE. The effect of the laser beam intensity profile in laser-based directed energy deposition: a high-fidelity thermal-fluid modeling approach. Addit Manuf 2024;86:104227. https://doi.org/10.1016/j.addma.2024.104227.

[2] Lian Y, Lin S, Yan W, Liu WK, Wagner GJ. A parallelized three-dimensional cellular automaton model for grain growth during additive manufacturing. Comput Mech 2018;61:543–58. https://doi.org/10.1007/s00466-017-1535-8.

[3] Jin K, Chen P, Feng P. Modeling for evaluating the effect of powder flow during laser cladding process: from thermal and flow fields to microstructure of the molten pool. Surf Coating Technol 2023;469:129799. https://doi.org/10.1016/j.surfcoat.2023.129799.

[4] Teferra K, Rowenhorst DJ. Optimizing the cellular automata finite element model for additive manufacturing to simulate large microstructures. Acta Mater 2021; 213:116930. https://doi.org/10.1016/j.actamat.2021.116930.

[5] Jin K, Yang Z, Chen P, Feng P, Qiao X. Modeling of solidification process during multi-track laser cladding with 3D cellular automata coupling gas-liquid interface tracking and solute suppression nucleation. J Mater Process Technol 2023;315: 117927. https://doi.org/10.1016/j.jmatprotec.2023.117927.

[6] Higashi M, Ozaki T. Selective laser melting of pure molybdenum: evolution of defect and crystallographic texture with process parameters. Mater Des 2020;191: 108588. https://doi.org/10.1016/j.matdes.2020.108588.

[7] Chlebus E, Gruber K, Kuźnicka B, Kurzac J, Kurzynowski T. Effect of heat treatment on the microstructure and mechanical properties of Inconel 718 processed by selective laser melting. Materials Science and Engineering: A 2015;639:647–55. https://doi.org/10.1016/j.msea.2015.05.035.

[8] Rivera OG, Allison PG, Brewer LN, Rodriguez OL, Jordon JB, Liu T, Whittington WR, Martens RL, McClelland Z, Mason CJT, Garcia L, Su JQ, Hardwick N. Influence of texture and grain refinement on the mechanical behavior of AA2219 fabricated by high shear solid state material deposition. Materials Science and Engineering: A 2018;724:547–58. https://doi.org/10.1016/j.msea.2018.03.088.

[9] Wang A, Wei Q, Luo S, Tang Z, Yang H, Wu Y, Leung CLA, Lee PD, Wang H, Wang H. Blue laser directed energy deposition of aluminum with synchronously enhanced efficiency and quality. Additive Manufacturing Letters 2023;5:100127. https://doi.org/10.1016/j.addlet.2023.100127.

[10] Dass A, Moridi A. State of the art in directed energy deposition: from additive manufacturing to materials design. Coatings 2019;9:418. https://doi.org/10.3390/coatings9070418.

[11] Lian Y, Gan Z, Yu C, Kats D, Liu WK, Wagner GJ. A cellular automaton finite volume method for microstructure evolution during additive manufacturing. Mater Des 2019;169:107672. https://doi.org/10.1016/j.matdes.2019.107672.

[12] Yuan L, Fattebert J-L, Sun C, Sabau AS. Uncovering grain and subgrain microstructure at the scale of additive manufacturing melt tracks with a scalable cellular automaton solidification model. Addit Manuf 2024;92:104401. https://doi.org/10.1016/j.addma.2024.104401.

[13] Zinovieva O, Zinoviev A, Romanova V, Balokhonov R. Three-dimensional analysis of grain structure and texture of additively manufactured 316L austenitic stainless steel. Addit Manuf 2020;36:101521. https://doi.org/10.1016/j.addma.2020.101521.

[14] McElfresh C, Marian J. Investigation of microstructures produced by metal additive manufacturing using 3D cellular automata finite element modeling in 316L steels and IN625 superalloys. J Mater Res Technol 2025;35:4301–14. https://doi.org/10.1016/j.jmrt.2025.01.247.

[15] Zinovieva O, Zinoviev A, Patel MN, Molotnikov A, Easton MA. Modelling grain refinement under additive manufacturing solidification conditions using high performance cellular automata. Mater Des 2024;245:113248. https://doi.org/10.1016/j.matdes.2024.113248.

[16] Bremer SJL, Luckabauer M, Römer GRBE. Laser intensity profile as a means to steer microstructure of deposited tracks in directed energy deposition. Mater Des 2023; 227:111725. https://doi.org/10.1016/j.matdes.2023.111725.

[17] Liu D-R, Wang S, Yan W. Grain structure evolution in transition-mode melting in direct energy deposition. Mater Des 2020;194:108919. https://doi.org/10.1016/j.matdes.2020.108919.

[18] Shi R, Khairallah SA, Roehling TT, Heo TW, McKeown JT, Matthews MJ. Microstructural control in metal laser powder bed fusion additive manufacturing using laser beam shaping strategy. Acta Mater 2020;184:284–305. https://doi.org/10.1016/j.actamat.2019.11.053.

[19] Baumard A, Ayrault D, Fandeur O, Bordreuil C, Deschaux-Beaume F. Numerical prediction of grain structure formation during laser powder bed fusion of 316 L stainless steel. Mater Des 2021;199:109434. https://doi.org/10.1016/j.matdes.2020.109434.

[20] Zhang Y, Zhang J. Modeling of solidification microstructure evolution in laser powder bed fusion fabricated 316L stainless steel using combined computational fluid dynamics and cellular automata. Addit Manuf 2019;28:750–65. https://doi.org/10.1016/j.addma.2019.06.024.

[21] Xiong F, Huang C, Kafka OL, Lian Y, Yan W, Chen M, Fang D. Grain growth prediction in selective electron beam melting of Ti-6Al-4V with a cellular automaton method. Mater Des 2021;199:109410. https://doi.org/10.1016/j.matdes.2020.109410.

[22] Babuska TF, Krick BA, Susan DF, Kustas AB. Comparison of powder bed fusion and directed energy deposition for tailoring mechanical properties of traditionally brittle alloys. Manufacturing Letters 2021;28:30–4. https://doi.org/10.1016/j.mfglet.2021.02.003.

[23] Wang Z, Zeng L, Lin X, Wang J, Feng Z, Dang C, Li H, Wang Y, Huang W. Microstructural evolution and strengthening mechanisms of additively-manufactured Al-Mg-Sc-Zr alloys: laser directed energy deposition versus laser powder bed fusion. J Alloys Compd 2024;985:173946. https://doi.org/10.1016/j.jallcom.2024.173946.

[24] Aziz U, McAfee M, Manolakis I, Timmons N, Tormey D. A review of optimization of additively manufactured 316/316L stainless steel process parameters, post-processing strategies, and defect mitigation. Materials 2025;18:2870. https://doi.org/10.3390/ma18122870.

[25] Chechik L, Sattari M, Römer GRBE, Schmidt M. Improved laser beam shapes for DED-LB/M: low-fidelity Monte-Carlo design and high-fidelity verification. Addit Manuf 2025;113:105016. https://doi.org/10.1016/j.addma.2025.105016.

[26] Li E, Shen H, Wang L, Wang G, Zhou Z. Laser shape variation influence on melt pool dynamics and solidification microstructure in laser powder bed fusion. Additive Manufacturing Letters 2023;6:100141. https://doi.org/10.1016/j.addlet.2023.100141.

[27] Bayat M, Rothfelder R, Schwarzkopf K, Zinoviev A, Zinovieva O, Spurk C, Hummel M, Olowinsky A, Beckmann F, Moosmann J, Schmidt M, Hattel JH. Exploring spatial beam shaping in laser powder bed fusion: High-fidelity simulation and in-situ monitoring. Addit Manuf 2024;93:104420. https://doi.org/10.1016/j.addma.2024.104420.

[28] Bakhtari AR, Sezer HK, Canyurt OE, Eren O, Shah M, Marimuthu S. A review on laser beam shaping application in laser-powder bed fusion. Adv Eng Mater 2024; 26:2302013. https://doi.org/10.1002/adem.202302013.

[29] Xie F, Zhai C, Zhang X, Emre A, Zheng H, Zhang X, Jiang S, Li X, Wu F, Hua X. Microstructure, dislocation and high-temperature oxidation behavior of as-cladding NiCoFeCrMo high-entropy alloy coatings: laser cladding vs vacuum cladding. J Alloys Compd 2025;1033:181278. https://doi.org/10.1016/j.jallcom.2025.181278.

[30] Xie F, Zhai C, Zhang X, Emre A, Cai G, Zhang X, Jiang S, Li X. Enhanced high-temperature oxidation resistance of TP347H supercritical boiler steel via vacuum cladding HEA coating at 800 °C. Surf Coating Technol 2025;496:131708. https://doi.org/10.1016/j.surfcoat.2024.131708.

[31] Xie F, Zhang X, Zhai C, Jiang S, Emre A, Zhang X, Hua X. Microstructure evolution and electrochemical corrosion behavior of FeCrCoNiMoB1.1Si1.2 high-entropy alloy coating via laser cladding. Electrochim Acta 2024;507:145153. https://doi.org/10.1016/j.electacta.2024.145153.

[32] Küçük Y, Altaş E, Topcu ME. A comparative analysis of the effect of laser surface treatment on the dry sliding wear behavior of ductile cast irons with different microstructures. Optik 2023;274:170540. https://doi.org/10.1016/j.ijleo.2023.170540.

[33] Altas E, Bati S, Rajendrachari S, Erkan Ö, Dag IE, Avar B. Comprehensive analysis of mechanical properties, wear, and corrosion behavior of AA7075-T6 alloy subjected to cryogenic treatment for aviation and defense applications. Surf Coating Technol 2024;490:131101. https://doi.org/10.1016/j.surfcoat.2024.131101.

[34] Schmidt M, Cvecek K, Duflou J, Vollertsen F, Arnold CB, Matthews MJ. Dynamic beam shaping—Improving laser materials processing via feature synchronous energy coupling. CIRP Ann 2024;73:533–59. https://doi.org/10.1016/j.cirp.2024.05.005.

[35] Dickey FM, editor. Laser beam shaping: theory and techniques. second ed., 0 ed. CRC Press; 2018. https://doi.org/10.1201/b17140.

[36] Vidergar A, Jeromen A, Govekar E. Influence of the laser-beam intensity distribution on the performance of directed energy deposition of an axially fed metal powder. J Mater Process Technol 2024;327:118360. https://doi.org/10.1016/j.jmatprotec.2024.118360.

[37] Tumkur TU, Voisin T, Shi R, Depond PJ, Roehling TT, Wu S, Crumb MF, Roehling JD, Guss G, Khairallah SA, Matthews MJ. Nondiffractive beam shaping for enhanced optothermal control in metal additive manufacturing. Sci Adv 2021; 7:9358. https://doi.org/10.1126/sciadv.abg9358.

[38] Gandin Ch-A, Desbiolles J-L, Rappaz M, Thevoz Ph. A three-dimensional cellular automation-finite element model for the prediction of solidification grain structures. Metall Mater Trans A 1999;30:3153–65. https://doi.org/10.1007/s11661-999-0226-2.

[39] Carozzani T, Gandin C-A, Digonnet H. Optimized parallel computing for cellular automaton–finite element modeling of solidification grain structures, Modelling Simul. Mater Sci Eng 2014;22:015012. https://doi.org/10.1088/0965-0393/22/1/015012.

[40] Zhang Y, Zhou J, Yin Y, Shen X, Shehabeldeen TA, Ji X. GPU-accelerated cellular automaton model for grain growth during directional solidification of nickel-based superalloy. Metals 2021;11:298. https://doi.org/10.3390/met11020298.

[41] Gu H, Fu Y, Wei C, Li L, Qian L, Zhou W, Li Y, Ren X. The impact of thermocapillary on equiaxed/columnar microstructure evolution in laser powder bed fusion: a high-fidelity ray-tracing based finite volume and cellular automaton study. J Mater Process Technol 2024;326:118335. https://doi.org/10.1016/j.jmatprotec.2024.118335.

[42] Heo TW, Khairallah SA, Shi R, Berry J, Perron A, Calta NP, Martin AA, Barton NR, Roehling J, Roehling T, Fattebert J-L, Anderson A, Nichols AL, Wopschall S, King WE, McKeown JT, Matthews MJ. A mesoscopic digital twin that bridges length and time scales for control of additively manufactured metal microstructures. J Phys Mater 2021;4:034012. https://doi.org/10.1088/2515-7639/abeef8.

[43] Ma J, Niu X, Zhou Y, Li W, Liu Y, Shen M, Wang H, Cheng W, You Z. Simulation of solidification microstructure evolution of 316L stainless steel fabricated by selective laser melting using a coupled model of smooth particle hydrodynamics and cellular automata. J Mater Res Technol 2023;27:600–16. https://doi.org/10.1016/j.jmrt.2023.09.296.

[44] Xiong F, Gan Z, Chen J, Lian Y. Evaluate the effect of melt pool convection on grain structure of IN625 in laser melting process using experimentally validated process-structure modeling. J Mater Process Technol 2022;303:117538. https://doi.org/10.1016/j.jmatprotec.2022.117538.

[45] Xue C, Blanc N, Soulié F, Bordreuil C, Deschaux-Beaume F, Guillemot G, Bellet M, Gandin C-A. Structure and texture simulations in fusion welding processes – comparison with experimental data. Materialia 2022;21:101305. https://doi.org/10.1016/j.mtla.2021.101305.

[46] Rolchigo M, Stump B, Coleman J, Reeve ST, Knapp GL, Plotkowski A. On the numerical sensitivity of cellular automata grain structure predictions to large thermal gradients and cooling rates. Comput Mater Sci 2025;249:113648. https://doi.org/10.1016/j.commatsci.2024.113648.

[47] Ebrahimi A. MoltenMetal oscillatory behaviour: in advanced Fusion-basedManufacturing processes. Delft University of Technology; 2022. https://doi.org/10.4233/UUID:06FF0B5E-D5DA-4149-A90F-62064C29F238.

[48] Gandin Ch-A, Rappaz M, Tintillier R. Three-dimensional probabilistic simulation of solidification grain structures: application to superalloy precision castings. Metall Trans A 1993;24:467–79. https://doi.org/10.1007/BF02657334.

[49] Edelsbrunner H, Kirkpatrick D, Seidel R. On the shape of a set of points in the plane. IEEE Trans Inf Theor 1983;29:551–9. https://doi.org/10.1109/TIT.1983.1056714.

[50] Gardiner JD, Behnsen J, Brassey CA. Alpha shapes: determining 3D shape complexity across morphologically diverse structures. BMC Evol Biol 2018;18:184. https://doi.org/10.1186/s12862-018-1305-z.

[51] Delaunay B. Sur la sphère vide, Izvestia Akademii Nauk SSSR. Otdelenie Matematicheskikh i Estestvennykh Nauk 1934;7:793–800.

[52] Coxeter HSM. Introduction to geometry. In: Wiley classics library edition. 2. New York: Wiley; 1989.

[53] Liang X, Zhu J, Popovich V, Hermans M, Richardson I, Bos C. A multi-level capture algorithm for accelerating cellular automata predictions of grain structure and texture in additive manufacturing. Addit Manuf 2025;98:104622. https://doi.org/10.1016/j.addma.2024.104622.

[54] Gandin Ch-A, Rappaz M. A 3D cellular automaton algorithm for the prediction of dendritic grain growth. Acta Mater 1997;45:2187–95. https://doi.org/10.1016/S1359-6454(96)00303-5.

[55] Bunge H-J. Texture analysis in materials science: mathematical methods. Burlington: Elsevier Science; 2013.

[56] Rolchigo M, Stump B, Belak J, Plotkowski A. Sparse thermal data for cellular automata modeling of grain structure in additive manufacturing, Modelling Simul. Mater Sci Eng 2020;28:065003. https://doi.org/10.1088/1361-651X/ab9734.

[57] Önel S, Ando T. Comparison and extension of free dendritic growth models through application to a Ag-15 mass pct Cu alloy. Metall Mater Trans 2008;39:2449–58. https://doi.org/10.1007/s11661-008-9568-4.

[58] Liu N, Liu F, Yang GC, Chen YZ, Yang CL, Li JS, Zhou YH. Dendrite growth in undercooled Fe–Co melt. J Alloys Compd 2008;455:L6–9. https://doi.org/10.1016/j.jallcom.2007.01.118.

[59] Chen Q, Shen H. Direct macroscopic modeling of grain structure and macrosegregation with a cellular automaton–finite element model. Metals 2019;9:177. https://doi.org/10.3390/met9020177.

[60] Aziz MJ. Model for solute redistribution during rapid solidification. J Appl Phys 1982;53:1158–68. https://doi.org/10.1063/1.329867.

[61] Lipton J, Kurz W, Trivedi R. Rapid dendrite growth in undercooled alloys. Acta Metall 1987;35:957–64. https://doi.org/10.1016/0001-6160(87)90174-X.

[62] Ludwig A. The interface response-functions in multi-componental alloy solidification. Phys Nonlinear Phenom 1998;124:271–84. https://doi.org/10.1016/S0167-2789(98)00202-4.

[63] Cook SJ, Clancy P. Impurity segregation in Lennard-Jones *A/AB* heterostructures. I. The effect of lattice strain. J Chem Phys 1993;99:2175–91. https://doi.org/10.1063/1.465280.

[64] JMatPro®. 2022. https://www.sentesoftware.co.uk/jmatpro/full-details.

[65] Pinomaa T, Lindroos M, Walbrühl M, Provatas N, Laukkanen A. The significance of spatial length scales and solute segregation in strengthening rapid solidification microstructures of 316L stainless steel. Acta Mater 2020;184:1–16. https://doi.org/10.1016/j.actamat.2019.10.044.

[66] Wang W, Shi Q, Zhu X, Liu Y. Numerical simulation of microstructure evolution in solidification process of ferritic stainless steel with cellular automaton. Crystals 2021;11:309. https://doi.org/10.3390/cryst11030309.

[67] Zinoviev A, Zinovieva O, Ploshikhin V, Romanova V, Balokhonov R. Evolution of grain structure during laser additive manufacturing. Simulation by a cellular automata method. Mater Des 2016;106:321–9. https://doi.org/10.1016/j.matdes.2016.05.125.

[68] Wu L, Zhu Y, Wang H, Li M. Crystal–melt interface kinetic behaviors of iron. AIP Adv 2021;11:035241. https://doi.org/10.1063/5.0041642.

[69] Gerstgrasser M, Jakob R, Pandya KS, Stirnimann J, Wegener K. CA single track microstructure simulation of nickel base alloy CM247LC and stainless steel S316L, including experimental validation of S316L. Mater Des 2021;199:109395. https://doi.org/10.1016/j.matdes.2020.109395.

[70] Zinovieva O, Zinoviev A, Ploshikhin V. Three-dimensional modeling of the microstructure evolution during metal additive manufacturing. Comput Mater Sci 2018;141:207–20. https://doi.org/10.1016/j.commatsci.2017.09.018.

[71] Ebrahimi A, Sattari M, Bremer SJL, Luckabauer M, Römer GRBE, Richardson IM, Kleijn CR, Hermans MJM. The influence of laser characteristics on internal flow behaviour in laser melting of metallic substrates. Mater Des 2022;214:110385. https://doi.org/10.1016/j.matdes.2022.110385.

[72] Ebrahimi A, Sattari M, Babu A, Sood A, Römer G-WRBE, Hermans MJM. Revealing the effects of laser beam shaping on melt pool behaviour in conduction-mode laser melting. J Mater Res Technol 2023;27:3955–67. https://doi.org/10.1016/j.jmrt.2023.11.046.

[73] MATLAB. https://www.mathworks.com; 2024.

[74] Bachmann F, Hielscher R, Schaeben H. Texture analysis with MTEX – free and open source software toolbox. Solid State Phenom 2010;160:63–8. https://dx.doi.org/10.4028/www.scientific.net/SSP.160.63.

[75] Li X, Tan W. Numerical investigation of effects of nucleation mechanisms on grain structure in metal additive manufacturing. Comput Mater Sci 2018;153:159–69. https://doi.org/10.1016/j.commatsci.2018.06.019.

[76] Morawiec A. On the magnitude of error in determination of rotation axes. J Appl Crystallogr 2024;57:1059–66. https://doi.org/10.1107/S1600576724004692.

[77] Klosek V. Crystallographic textures. EPJ Web Conf 2017;155:00005. https://doi.org/10.1051/epjconf/201715500005.

[78] Creuziger A, Calhoun CA, Poling WA, Gnäupel-Herold T. Assessment of bias errors caused by texture and sampling methods in diffraction-based steel phase measurements. J Appl Crystallogr 2018;51:720–31. https://doi.org/10.1107/S160057671800420X.

[79] Massey FJ. The kolmogorov-smirnov test for goodness of fit. J Am Stat Assoc 1951; 46:68–78. https://doi.org/10.1080/01621459.1951.10500769.

[80] Hunt JD. Steady state columnar and equiaxed growth of dendrites and eutectic. Mater Sci Eng 1984;65:75–83. https://doi.org/10.1016/0025-5416(84)90201-5.

[81] Meier C, Penny RW, Zou Y, Gibbs JS, Hart AJ. Thermophysical phenomena in metal additive manufacturing by selective laser melting: fundamentals, modeling, simulation, and experimentation. Annual Review of Heat Transfer 2017;20: 241–316. https://doi.org/10.1615/AnnualRevHeatTransfer.2018019042.

[82] Baghjari SH, AkbariMousavi SAA. Experimental investigation on dissimilar pulsed Nd:YAG laser welding of AISI 420 stainless steel to kovar alloy. Mater Des 2014;57: 128–34. https://doi.org/10.1016/j.matdes.2013.12.050.